Mineralogy and Petrology (2024) 118:345–366
https://doi.org/10.1007/s00710-024-00863-4

RESEARCH

Geochemistry of apatites from preshield and postshield basalts and their petrogenetic implications: A case study of the Naitoushan basalt and Heishigou dike in the Changbaishan Tianchi volcano, NE China

Zhitao Xu[1,2,3,4,5] · Liying Sun[3] · Xiqing Ye[1,2] · Mengmeng Li[2] · Xiaodong Pan[3] · Yujia Song[3]

Received: 6 April 2023 / Accepted: 19 June 2024 / Published online: 18 July 2024

Abstract

In this study, laser ablation–multicollector–inductively coupled plasma–mass spectrometry (LA–MC–ICP–MS) of apatites and LA–ICP–MS of zircons are used to collect U–Pb geochronological data, Rb–Sr isotope chronology is used to analyze alkaline feldspar and plagioclase, and archival apatite geochemistry data for the exposed Naitoushan basalt and Heishigou dike in the Changbaishan Tianchi volcano (CTV) are accessed to examine the petrogenesis and determine the origin of basaltic magmatism in the CTV. The Naitoushan basalt and Heishigou dike formed at 22.2–18.7 and 0.230–0.218 Ma, respectively. In situ oxides, volatiles, trace element geochemistry and Sr–Nd isotopes of apatite are reported for two samples. Most apatites are in the early crystallization phase and form inclusions in plagioclase that are euhedral or subhedral. They have higher MgO and K_2O/Na_2O concentrations; lower F and Cl concentrations; Ba, Sr, Nb, Ta, Zr, Hf, K, and Ti depletion; and Th, U, Ce, Pb, P, and Nd enrichment. All apatite samples are enriched in light rare earth elements (REEs) relative to heavy REEs and have relatively homogeneous Th/U, Zr/Hf, La/Sm, and Nd/Tb ratios and Sr–Nd isotopic compositions; thus, their host magmas potentially have the same magmatic origin as oceanic island basalt. The apatite La, Yb, and U contents, Eu/Eu* and La/Yb values, and high REE contents show a weak crystallization sequence in the mafic magma. This study demonstrates that the pre-shield and post-shield mafic magmas in the CTV were likely derived from an enriched mantle source with an I-type signature related to the rollback of the Pacific plate.

Keywords Apatite geochemistry · Basalt · Petrogenesis · Magma source · Changbaishan Tianchi volcano

Introduction

The eastern block in China contains the eastern part of the Central Asian orogenic belt (CAOB), North China craton (NCC) (Fig. 1a), Sulu–Dabie orogenic belt, Yangtze craton, and southeastern coastal orogenic belt of China (Fig. 1b) (Sun et al. 2022); this area is characterized by widespread Mesozoic–Cenozoic volcanic rocks, subvolcanic rocks, and intrusive rocks. The late Cenozoic volcanic rocks are mainly composed of alkaline basalts that erupted in an intraplate environment (Chen et al. 2017). They are mainly distributed in the eastern margin of the CAOB and Northeast China, with the Changbaishan volcanic field (CVF) rocks being the most widely distributed. The CVF consists of basalt shields, monogenic vents, and composite central volcanoes (Li et al. 2021a, b). In the last ten years, seismic and three–dimensional magnetotelluric imaging has revealed that the CTV is located above the 500 km deep stagnant plate of the western part of the subducting Pacific plate (Yang et al. 2021; Song

Editorial handling: M.A.T.M Broekmans

✉ Zhitao Xu
xuzhjtao@163.com

✉ Xiaodong Pan
panxd1970@126.com

1 Institute of Volcanology, China Earthquake Administration, Changchun 130117, China

2 Jilin Changbaishan Volcano National Observation and Research Station, Institute of Geology, China Earthquake Administration, Beijing 100029, China

3 Jilin Earthquake Agency, Changchun 130117, China

4 Istituto Nazionale di Geofisica e Vulcanologia, Rome 00143, Italy

5 Istituto Nazionale di Geofisica e Vulcanologia, Osservatorio Vesuviano, Napoli 80124, Italy

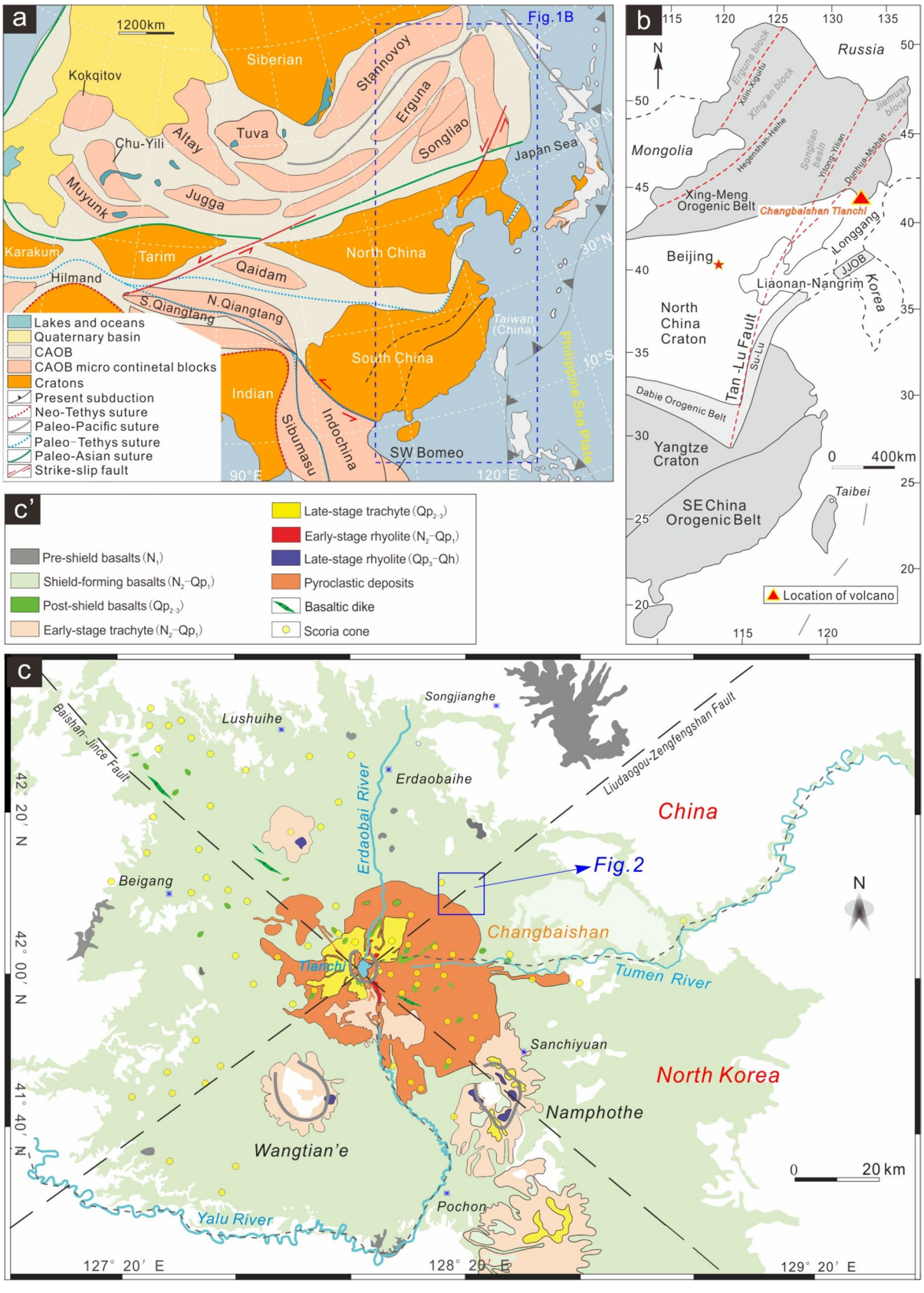
a
1200km
Fig.1B
Kokqitov
Siberian
Stannovoy
Erguna
Songliao
Chu-Yili
Altay
Tuva
Muyunk
Jugga
Japan Sea
Karakum
Tarim
Qaidam
North China
Hilmand
S.Qiangtang
N.Qiangtang
Taiwan (China)
South China
Indian
Sibumasu
Indochina
SW Bomeo
Philippine Sea Plate
Lakes and oceans
Quaternary basin
CAOB
CAOB micro continetal blocks
Cratons
Present subduction
Neo-Tethys suture
Paleo-Pacific suture
Paleo-Tethys suture
Paleo-Asian suture
Strike-slip fault
b
Russia
Mongolia
Erguna block
Xilin-Xiguiti
Xing'an block
Hegenshan-Heihe
Songliao basin
Yitong-Yilan
Dunhua-Mishan
Jiamusi block
Xing-Meng Orogenic Belt
Changbaishan Tianchi
Beijing
Longgang
JJOB
Liaonan-Nangrim
Korea
North China Craton
Tan-Lu Fault
Su-Lu
Dabie Orogenic Belt
Yangtze Craton
SE China Orogenic Belt
Taibei
0 400km
Location of volcano
c'
Pre-shield basalts (N1)
Shield-forming basalts (N2–Qp1)
Post-shield basalts (Qp2-3)
Early-stage trachyte (N2–Qp1)
Late-stage trachyte (Qp2-3)
Early-stage rhyolite (N2–Qp1)
Late-stage rhyolite (Qp3–Qh)
Pyroclastic deposits
Basaltic dike
Scoria cone
c
Songjianghe
Lushuihe
Baishan-Jince Fault
Erdaobaihe
Erdaobai River
Liudaogou-Zengfengshan Fault
China
Fig.2
Beigang
Changbaishan
Tianchi
Tumen River
Sanchiyuan
North Korea
Namphothe
Wangtian'e
Pochon
Yalu River
0 20 km
42° 20′ N
42° 00′ N
41° 40′ N
127° 20′ E
128° 20′ E
129° 20′ E

◂**Fig. 1** **a** Map showing the tectonic framework of the main subdivisions of central and eastern Asia, as well as eastern China (modified after Zhou et al. 2018); **b** simplified tectonic units of eastern China and the location of the CVF (modified according to Xu et al. 2012); **c** regional geological map of the CVF (Li et al. 2021a, b)

and Lei 2023). Three geodynamic mechanisms have been proposed to explain large-scale basaltic magmatic eruptions in the CVF: upwelling mantle plumes (Chen et al. 2007), intraplate continental rifting (Gilder et al. 1991; Dong et al. 2023) and Pacific plate subduction (Zhang et al. 2018). More studies on volcanism have focused on the Millennium eruption (ME) (Zou et al. 2014; Pan et al. 2020), and minimal attention has been given to the chronology, single mineral geochemistry and related magmatic stages or genesis of basalts in the CVF. There are different views on the nature or origin of shield-formed and postshield basaltic magmas in the CVF: 1) partial melting of asthenospheric mantle, with contamination by crustal material (Li et al. 2021a, b); 2) partial melting of the subducting Pacific plate (Zou et al. 2008; Ma et al. 2019); 3) involvement of depleted mantle (DM) and enriched mantle I-type (EM I) (Basu et al. 1991) or involvement of oceanic island basalt (OIB) and EMI materials (Choi et al. 2014; Chen et al. 2021); 4) an asthenospheric mantle source that is involved in subducted sediments or originated from subcontinental lithospheric mantle or has the characteristics of mid-ocean ridge basalt (MORB) (Choi et al. 2020); and 5) similar to the EMI source, derived from the contamination of OIB-type mantle by Paleoproterozoic lithospheric crust (Lee et al. 2021).

Apatite ($Ca_5[PO_4]_3[F, Cl, OH]$) is a low-temperature accessory mineral that is widely developed in the volcanic rocks of the CTV, and its U–Pb sealing temperature (450 °C–550 °C) is lower than that of zircon (700 °C–900 °C). The mineral lattice of apatite is often rich in Sr, Mn, Mg, rare earth elements (REEs), Hf, Pb, U, Th and other elements. This information, combined with isotope geochemical data, can also provide specific rock ages and genetic information (Cherniak 2005). Palma et al. (2019) and Broom et al. (2017) suggested that apatite could be used as a powerful tool for resolving complex magmatic activity and that apatite that crystallizes from magmas with different components does not undergo isotopic changes in the host rock. The geochemistry of associated apatite effectively records the magma source and possible magmatic activity (Chu et al. 2009; Laurent et al. 2017). The CVF is composed of massive late Cenozoic basaltic, trachytic and alkaline rhyolitic volcanic rocks. The following are unresolved issues regarding the preshield and postshield basaltic magmatic eruption of the CTV: 1) whether they were products of continuous or multiple intermittent eruptions from the same magma chamber; 2) whether the eruption of magma was caused by the evolution of the magma itself (such as the fractional crystallization of magma, volatiles and water content in magma, and magma mixing) or by other factors (such as regional deformation, the presence of faults, and the uneven thickness of the overlying crust); and 3) whether there were single or multiple magma sources. Furthermore, volcanic gases (such as CO_2, H_2S, and SO_2) are emitted from the CVF, all the rocks have undergone varying degrees of gas–liquid alteration (Aleinikoff et al. 2015; Mathieu et al. 2016), and the genesis/magmatic processes of these rocks cannot be clearly elucidated by only whole–rock geochemistry (Warren et al. 2007). Therefore, it is necessary to use new methods to evaluate the role of these basaltic magmatic evolutionary processes in the formation of basalts in the CVF.

The 22–18 Ma Naitoushan basalt and 0.23–0.22 Ma Heishigou dikes are located in the northeastern CTV, were emplaced together and are easily discoverable, providing us with an opportunity to study the above issues. In this study, we present new Rb–Sr dating results for alkaline feldspar and plagioclase, zircon and apatite U–Pb geochronological data and comprehensive in situ geochemical (main oxides, volatiles, trace elements and Sr–Nd isotopic compositions) analyses of apatite in combination with whole–rock geochemical data from preshield and postshield basalts in the CTV in Jilin Province, NE China. These results improve our understanding of basaltic magma sources and the role of magmatic processes in the petrogenesis of basalts.

Geological background and samples

The CTV is an active volcano located on the boundary between China and North Korea. Tectonically, it is the eastern margin of the CAOB, the northern margin of the NCC, and near the NE-striking regional Dunhua–Mishan fault (Fig. 1b). Several monogenetic scoria cones and dikes surround the CTV, and they align approximately in a NW–SE or NE–SW direction. This direction is the same as that of the main faults (Baishan–Jince or Tianchi–Zengfengshan fault) affecting the Tianchi caldera (Fig. 1c). The basement of the CTV consists of Archean and Proterozoic metamorphic rocks (Wang et al. 2003; Li et al. 2023).

In the preshield stage of the CTV, scattered monogenetic basaltic volcanoes widely developed across the Gaima Plateau (22–13 Ma), with limited parasitic basaltic monogenic volcanism occurring in the Tianchi cone, such as occurred with the early Miocene Naitoushan basalt (Figs. 1c and 2). The shield-forming eruptive materials of the CTV mainly comprise a series of basaltic volcanic rocks, from lower to upper: Quanyang basalt (5.02–4.26 Ma), Toudao (Baishan) basalt (2.77–1.48 Ma) and Laofangzixiaoshan basalt (1.17–0.75 Ma) (Wei et al. 2021). The construction of the CTV cone is composed mainly of trachytic and comenditic volcanic rocks, and their eruptions lasted throughout the

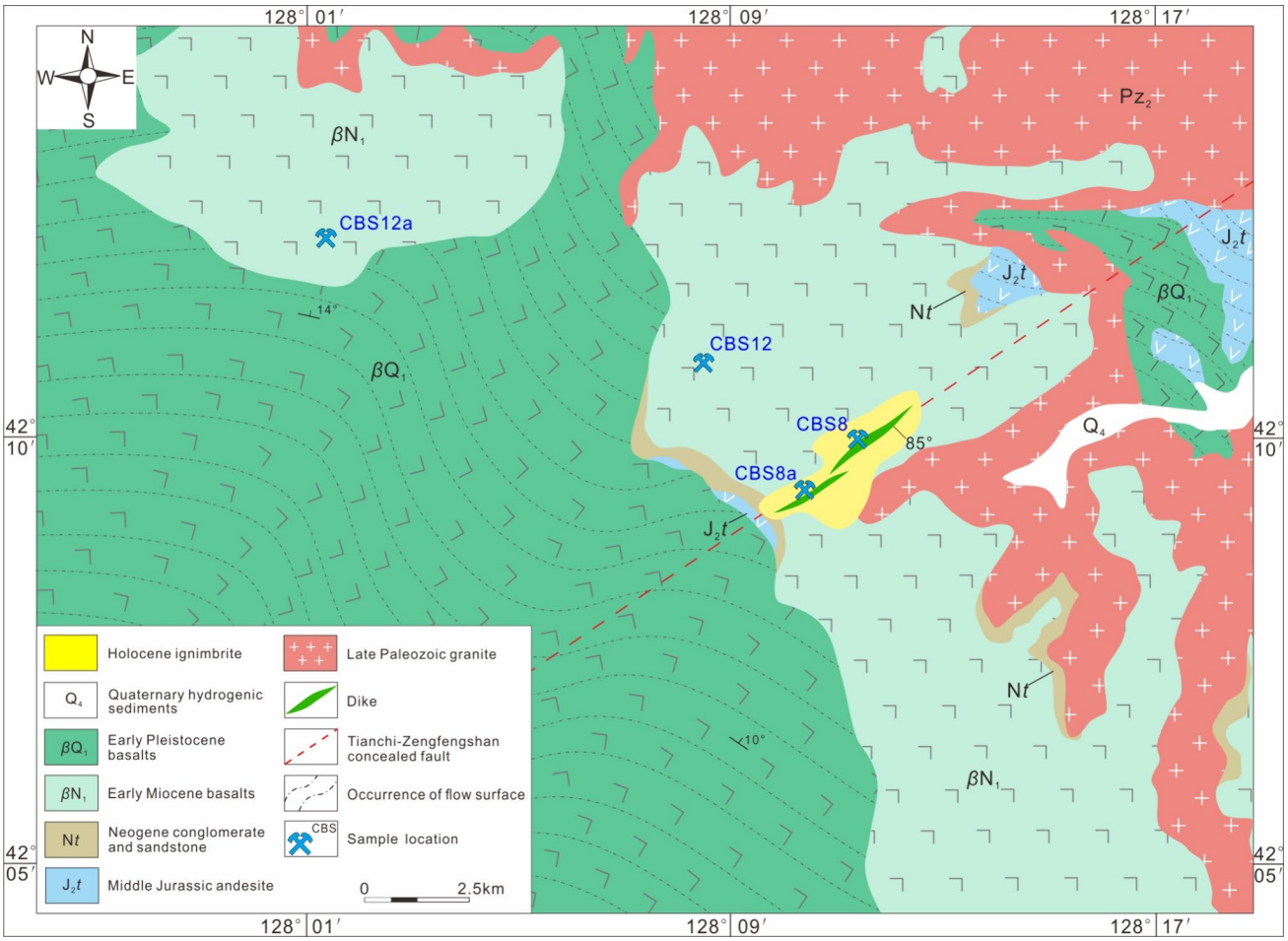

Fig. 2 Simplified geological map of the study area (after Yan et al. 2023)

Pleistocene (0.61–0.019 Ma), with small numbers of basaltic volcanic rocks, such as Heishigou basaltic dikes, forming in the postshield stage (Fig. 2). Before the formation of the Tianchi volcanic cone, small-scale intermediate–felsic magma erupted between 1.49 and 1.00 Ma. Postcaldera-forming and postcaldera eruptions mostly occurred between 900 and 1100 BP. The ME had several potential eruption ages, including 928, 939 and 946 AD. All the ME ages confirmed a likely tenth century eruption age, and the eruption resulted in mainly pumiceous ignimbrite deposits. The records of the 1903 eruption were limited to phreatomagmatic eruptions (Yatsuzuka et al. 2010).

Due to the certainties in the petrological relationship between the Naitoushan basalt and Heishigou dikes, we aim to better understand their magma sources and magmatic petrogenetic processes. Our samples were collected from those rocks (Fig. 2), and their key petrographic features and rock-forming mineral assemblages are summarized as follows:

1. The Naitoushan basalt constitutes the main body in the study area (Fig. 2) and is located in the northeastern part of the Tianchi volcanic area (Fig. 1c). The basalt has massive structures (Fig. 3a and c) and intergranular textures, with few pores. The major mineral assemblage includes plagioclase (60–65%), clinopyroxene (10–15%), olivine (5–10%), and alkali feldspar (5%), with accessory minerals such as apatite, Fe–Ti oxides, zircon, and monazite (5%) (Fig. 3e).
2. The Heishigou dikes are distributed in the northeastern part of the Tianchi volcanic cone (Figs. 1c and 2) and occur as dikes or as intrusions within the ignimbrite deposits and the Naitoushan basalt (Figs. 2 and 3b). The strike is NE, the dip angles are 70–85°, and the widths vary from 2.2–6.7 m. The pore content is approximately 15 vol%, and the sizes are 0.05–0.5 mm, indicating the degassing of magma near the surface (Fig. 3d). They are composed mainly of plagioclase (70–75%), alkali feldspar (5–10%), clinopyroxene (5–10%), olivine (5%) and accessory apatite, magnetite, titanite, phlogopite, zircon and monazite (5%) (Fig. 3f, f').

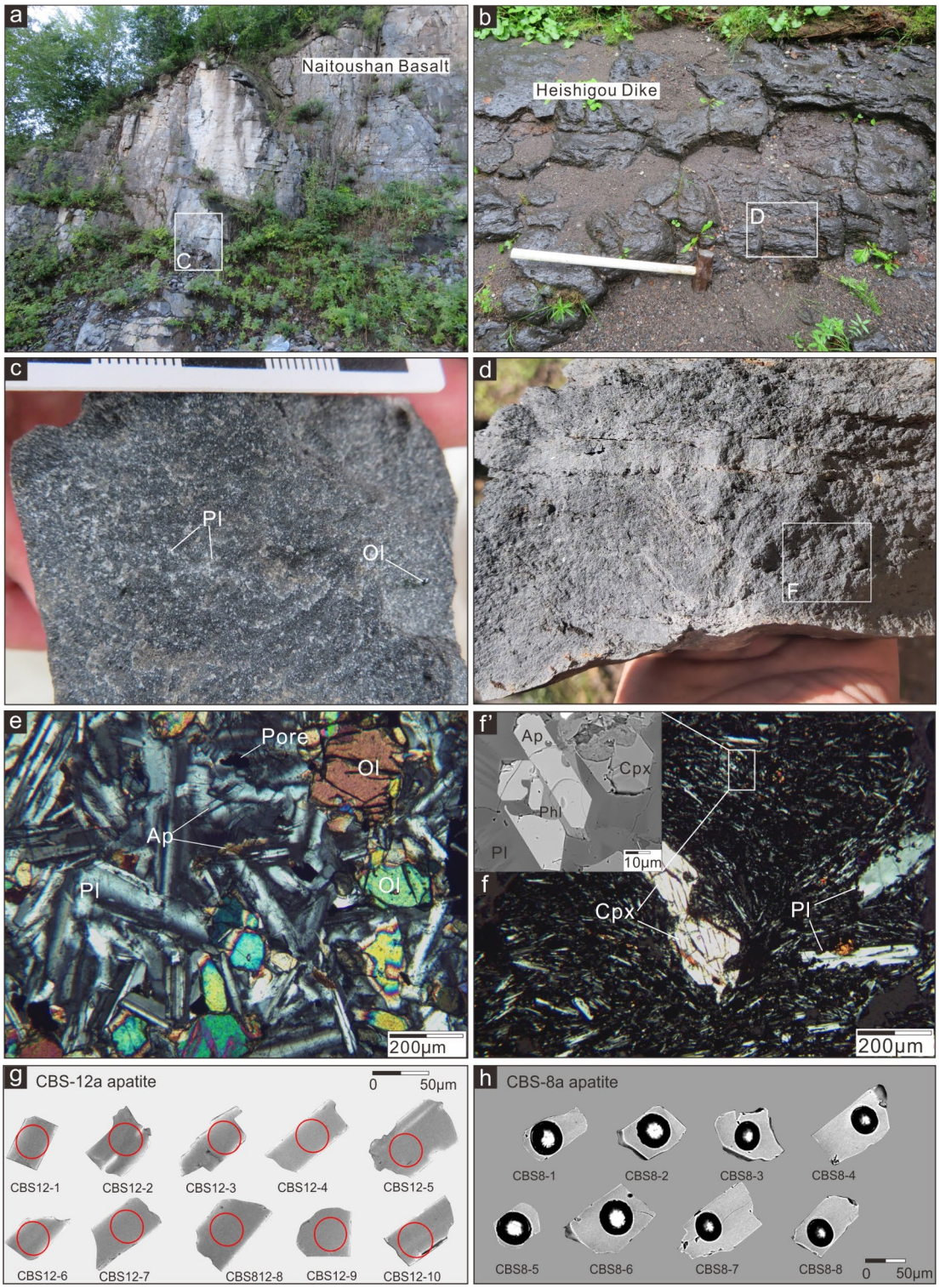

Fig. 3 **a** and **b** Representative field photographs showing outcrops of the Naitoushan basalt (CBS–12a) and Heishigou dike (CBS–8a). **c** and **d** Hand specimen photographs of representative samples. **e**, **f** and **f'** Photomicrographs of the Naitoushan basalt and Heishigou dike. **g** and **h** SEM–CL images of representative apatite grains from **e** and **f**. The circles indicate the locations of the EPMA and LA–ICP–MS analysis. Ap: apatite, Cpx: clinopyroxene, Ol: olivine, Phl: phlogopite, Pl: plagioclase

Analytical methods

Sampling and representativity

Apatite laser ablation–inductively coupled plasma–mass spectrometry (LA–ICP–MS) U–Pb dating samples were obtained from the Naitoushan basalt. We used an in situ sampling method and collected samples from homogeneous and weakly weathered parts of the rock (Fig. 3a, c). To ensure sufficient samples for testing, we collected 10.5 kg of fresh rock samples and cleaned them to prevent contamination. The zircon laser ablation–multicollector–inductively coupled plasma–mass spectrometry (LA–MC–ICP–MS) U–Pb and Rb–Sr dating samples were obtained from the Heishigou basaltic dike. We also used an in situ sampling method, and the samples were all from homogeneous and weakly weathered rocks (Fig. 3b, d). We collected a total of 15 kg of fresh rock samples; cleaned them to prevent contamination; and then cleaned, cut, broke, roughened, overmagnetized, electromagnetically treated and fine-panned the samples for in situ geochemical analysis of apatite and zircon.

Thin section preparation and optical petrography

The Naitoushan basalt and Heishigou basaltic dike samples used for probe testing were cut and numbered, heated in an oven with volatile water (85 ℃), mixed with resin adhesive and triethanolamine (5:1), and this mixture was applied evenly to the heated samples; the samples were subsequently heated for ten hours (85 ℃), followed by rough grinding and fine grinding and polishing to a thicknesses of 0.04–0.05 mm. The zircon and apatite were picked out under a microscope, the samples with good self-shapes and no fragmentation were attached, and the resin was fixed and polished until the apatite and zircon were exposed internally for analysis. Sample pretreatment and scanning electron microscopy cathodoluminescence (SEM–CL) imaging were performed at Nanjing Hongchuang Geological Exploration Technology Service Co., Ltd. (NHEXTS), Nanjing, China.

Mineral composition by EPMA

The current and beam spot used by the electron probe to test different minerals were different, i.e., 10 nA and 10 μm for feldspar, and 2 nA–5 nA and 20 μm for apatite. The same mineral was affected by the size, ring and other factors, and the current and beam spot used in different situations were different. The concentrations of apatite were determined using a JEOL JXA–8230 electron probe microanalysis (EPMA) instrument. The accelerating voltage, beam current and beam diameter were 15 kV, 5 nA and 20 μm, respectively. The peak counting times were 10 s for Si, Ti, Al, Fe, Mn, Mg, Ca, Na, K, P, F, and Cl and 20 s for S. The background counting time was half of the peak counting time. All the data were corrected for matrix effects using the ZAF correction method (Donovan and Tingle 1996; Cao et al. 2013). The following standards were used: jadeite (Si), rutile (Ti), yttrium Al garnet (Al), hematite (Fe), rhodonite (Mn), olivine (Mg), apatite (Ca), albite (Na), orthoclase (K), apatite (P), fluorite (F), tugtupite (Cl), and celestite (S). A 1–10 μm electron beam was used according to the size of the mineral shards, and the analytical uncertainties were less than 2%. The data are listed in Table 1.

Table 1 Main element oxides and volatile contents of CBS–12a and CBS–8a apatites by EMPA (wt%). FeO^T represents total iron (oxide) content

Sample	LLD	CBS-12a					CBS-8a				
Spot		1	2	3	4	5	1	2	3	4	5
SiO_2	??	0.29	0.29	0.17	0.12	0.49	0.28	0.28	0.25	0.2	0.21
Al_2O_3	??	<LLD	0.06	0.06	0.02	0.13	<LLD	<LLD	<LLD	<LLD	0.01
FeO^T	??	0.19	0.35	0.19	0.27	0.26	0.37	0.2	0.2	0.27	0.36
MnO	??	<LLD	0.05	0.04	0.07	0.02	0.01	0.07	<LLD	0.04	0.06
TiO_2	??	0.05	0.09	<LLD	0.03	<LLD	0.09	<LLD	<LLD	0.02	0.14
MgO	??	0.24	0.28	0.15	0.34	0.21	0.22	0.14	0.24	0.25	0.25
CaO	??	53.13	53.49	53.82	54.28	53.29	52.7	54.07	54.64	53.29	53.46
Na_2O	??	<LLD	0.05	0.08	0.04	0.07	0.06	0.01	<LLD	<LLD	0.05
K_2O	??	0.04	0.01	0.03	0.06	0.06	0.03	0.05	0.1	0.08	0.03
P_2O_5	??	42.85	42.87	42.22	42.54	42.6	42.83	42.61	42.86	42.41	42.57
SO_3	??	0.03	0.03	<LLD	<LLD	0.03	0.04	0.04	0.04	0.01	<LLD
F	??	2.06	2.21	2.42	2.8	2.8	2.92	2.93	2.99	3.26	3.4
Cl	??	0.24	0.36	0.26	0.28	0.27	0.37	0.3	0.28	0.32	0.31
Analytical total		98.2	99.12	98.37	99.59	98.99	98.6	99.41	100.28	98.7	99.35

Trace element contents of apatite by LA–ICP–MS (including Sr and Nd)

Trace element analysis and Sr–Nd isotope analysis were performed at Nanjing Hongchuang Geological Exploration Technology Service Co., Ltd. (NHEXTS), Nanjing, China. In situ trace element analysis of apatite was conducted using LA–ICP–MS. The analysis was completed in the super purification laboratory. The Resolution SE model laser ablation system (Applied Spectra, USA) was equipped with an ATL (ATLEX 300) excimer laser and a two-volume S155 ablation cell. The laser ablation system was coupled to an Agilent 7900 ICP–MS (Agilent, USA). The detailed tuning parameters are provided in Thompson et al. (2018). LA–ICP–MS tuning was performed using a 50 micron-diameter line scan at 3 µm/s on a NIST 612 instrument at ~ 3.5 J/cm^2 with a repetition rate of 10 Hz. The gas flow was adjusted to obtain the highest sensitivity (^{238}U ~ 6×10^5 cps) and the lowest oxide ratio (ThO/Th < 0.2%). P/A calibration was conducted with NIST 610 using a 100 micron-diameter line scan. Preablation was conducted for each spot analysis using 5 laser shots (~ 0.3 µm in depth) to remove potential surface contamination. The mass was analyzed with a total sweep time of ~ 0.26 s. The analysis was performed using a 38 µm-diameter spot at 5 Hz with a fluence of 3 J/cm^2. The Iolite software package was used for data reduction (Paton et al. 2011). NIST 610 and ^{43}Ca were used to calibrate the trace element concentrations as an external reference material and internal standard element, respectively. The analytical uncertainties were less than 2%. The data are presented in Tables 2 and 3, Supplementary Tables 1 and 2.

In situ Sr isotope measurements were performed on a Neptune Plus MC–ICP–MS (Thermo Fisher Scientific, USA) instrument in combination with a Resolution SE 193 nm laser ablation system (Applied Spectra, USA). The analysis was completed in the super purification laboratory. The MC–ICP–MS interface was modified using a high-efficiency dry pump to increase the ion transmission efficiency. The JET sample and X skimmer cones were used along with the guard electrode (GE). The Faraday cup configuration of the ion detection system was composed of an array from L_4 to H_3 aligned to monitor Kr, Rb, Er, Yb and Sr (Tong et al. 2016). The determined ^{87}Sr/^{86}Sr of the NBS 987 standard was 0.710245 ± 0.000025 (2σ, n = 12), which is consistent with the results determined via thermal ionization mass spectrometry (TIMS) with an ^{87}Sr/^{86}Sr of 0.710236 (Jochum et al. 2006; Paton et al. 2007; Yang et al. 2014a). The Durango apatite standard was analyzed every 10–15 samples to monitor the instrument stability.

In situ Nd isotope measurements were performed on a Neptune Plus MC–ICP–MS (Thermo Fisher Scientific, Germany) instrument in combination with a J–200 343 nm femtosecond laser ablation system (Applied Spectra, USA). The analysis was completed in the super purification laboratory. The JET sample and X skimmer cones were used along with the GE instrument. The instrumental mass bias for Nd and Sm isotopes was corrected using an exponential law function based on a ^{146}Nd/^{144}Nd value of 0.7219 and a ^{147}Sm/^{149}Sm value of 1.0868 (Yang et al. 2014b). The interferences of ^{143}Sm to ^{143}Nd were corrected based on the measured signal intensities of ^{147}Sm, mass bias coefficient and natural isotopic composition. The Durango apatite standard was analyzed for every 10 samples to monitor the instrument stability and external correction of ^{147}Sm/^{144}Nd ratios. The values of $(^{87}Sr/^{86}Sr)_i$, $(^{143}Nd/^{144}Nd)_i$ and εNd(t) were calculated from Lugmair and Marti (1978). The Sr–Nd isotope values are summarized in Table 4 and Supplementary Table 3.

U–Pb dating of apatite and zircon

Apatite LA–ICP–MS U–Pb dating was completed by Yanduzhongshi Geological Analysis Laboratories Ltd. (YGALL). The U−Pb dating of apatite in this study was performed in the super purification laboratory via an Analytik Jena M90 quadrupole laser ablation multicollector inductively coupled plasma−mass spectrometry (LA–ICP–MS) instrument with a 193 nm NWR193 Ar–F excimer laser. The downhole fractionation, instrument drift and mass bias correction factors for the Pb/U ratios in apatite were calculated using 2 analyses of the primary (MAD2 Cochrane et al. 2014) and secondary standard apatites. McClure Mt (Schoene and Bowring 2006), Otter Lake (Barfod et al. 2005) and Durango (McDowell et al. 2005) were analyzed at the beginning of the session and after every 10 unknown apatites using the same spot size and conditions as those used for the samples. The trace element contents of apatite were quantified using SRM610 as an external standard and ^{44}Ca as the internal standard element, assuming stochiometric proportions. Each analysis of apatite began with a 20 s blank gas measurement followed by a further 40 s analysis time when the laser was switched on. A flow of He carrier gas at a rate of 0.55 L/minute carried particles ablated by the laser out of the chamber to be mixed with Ar gas and to the plasma torch. The measured isotopes were ^{31}P, ^{44}Ca, ^{206}Pb, ^{207}Pb, ^{208}Pb, ^{232}Th, ^{235}U and ^{238}U; each element was measured every 0.18 s, with a longer counting time for Pb isotopes than for other elements. The data reduction that was used was based on the method outlined in detail in Meffre et al. (2008), with an additional modification to correct for the small amount of common Pb present in the primary standard using the ^{207}Pb correction of Chew et al. (2014). The results of the analyses are listed in Table 5 and Supplementary Tables 4 and 5.

Zircon U–Pb dating was conducted via LA–MC–ICP–MS. The Resolution SE model laser ablation system (Applied Spectra, USA) that was used was equipped with an ATL (ATLEX

Table 2 Trace element and rare-earth element contents in CBS–12a and CBS–8a apatites by LA–ICP–MS in parts per million (ppm, or μg·g-1)

		CBS-12a								CBS-8a							
Sample No	LLD	1	2	3	4	5	6	7	8	1	2	3	4	5	6	7	8
K	??	467	12.6	26.5	70.5	70	460	6.05	2.38	6.53	11.92	9.52	10.4	7.29	13.7	10.66	30.87
Ti	??	18.8	19.6	20.3	22.6	21.1	19.2	16.1	18.7	5.47	5	4.36	5.18	8.89	11.26	12.7	17.7
Rb	??	0.8	0.124	0.142	0.55	0.63	1.84	0.094	0.07	0.089	0.093	0.097	0.09	0.074	0.173	0.11	0.092
Sr	??	1325	1316	1320	1312	1247	1382	1356	1387	865	775.3	784.8	631.4	1193	622.9	987.5	579.2
Y	??	426.3	494.9	466.2	448.7	512	474.3	488.9	441.6	663.5	704.7	707.2	748	580.1	1321	694.9	899.7
Zr	??	16.5	19.36	25.9	19.32	18.08	19.45	19.65	18.58	18.02	16.23	18.79	18.22	20.07	32.5	19.3	31.76
Nb	??	0.178	0.09	0.35	0.266	0.092	0.083	0.073	0.073	0.066	0.062	0.061	0.072	0.061	0.105	0.081	0.107
Ba	??	35.8	34.53	33.19	31.23	30.4	35.4	34.3	33.2	19.91	19.66	18.51	13.72	22.18	17.95	22.46	15.65
Hf	??	0.081	0.082	0.07	0.081	0.084	0.08	0.058	0.06	0.077	0.066	0.06	0.071	0.078	0.146	0.08	0.121
Ta	??	0.0058	0.0009	0.00075	0.0093	0.0023	0.00048	0.00042	0.0023	0.00058	0.00029	0.00064	0.00027	0.00027	0.00058	0.00029	0.00064
Pb	??	1.001	0.988	1.023	1.064	1.38	1.13	1.205	1.162	0.786	0.831	0.799	0.93	0.597	0.982	0.69	0.943
Th	??	14.92	18.56	16.08	16.01	15.55	17.91	19.29	16.47	20	19.6	20.92	20.86	21.99	45.6	23.33	25.72
U	??	3.681	4.35	3.85	3.918	3.69	4.29	4.742	3.948	4.936	4.837	4.98	4.97	4.947	8.66	5.598	6.21
		rare-earth element (REE) contents (in ppm, or $\mu g \cdot g^{-1}$)															
La	??	620	725	675	636.3	791	690	737.3	639.2	1213	1311	1287	1343	996	2306	1240	1788
Ce	??	1375	1614	1507	1422	1788	1595	1694	1486	2746	2963	2899	3012	2281	5260	2801	3984
Pr	??	176.4	206.7	195.1	183.9	222.8	201.6	212.6	188.7	355.1	378.2	370.6	385.1	301.7	669	363.3	510.9
Nd	??	797	939	880	840.1	978	903	940.2	840.5	1581	1661	1645	1702	1387	2972	1633	2263
Sm	??	165.4	192.3	182	174.8	198.6	185.5	190.5	174.1	319.5	332.2	334.9	343	286.8	601	330.9	447.3
Eu	??	34.28	39.67	38.36	38.01	41.7	39.72	39.16	37.42	42.66	38.05	42.13	45.51	45.54	67.8	47.36	41.37
Gd	??	149.5	172.9	163.9	158	175.1	168.8	171.7	157	279	288.6	289.5	300.4	255.5	522	291.1	381.7
Tb	??	17.3	20.25	19.09	18.42	20.47	19.34	20.09	18.22	32.38	33.92	33.53	35.24	29.05	61.9	33.53	43.33
Dy	??	90.2	103.8	98.1	95.3	108.4	102.1	104.7	96.5	161.7	169.1	170	177.3	143.6	313.1	171.7	216.4
Ho	??	15.59	17.84	16.67	16.34	18.6	17.46	18.15	16.4	26.13	27.75	27.54	28.95	23.29	51.5	27.67	34.61
Er	??	36.66	42.56	39.83	39.03	44.3	41.27	43.27	38.54	58.48	62.29	63.21	65.5	51.23	116.6	61.28	75.17
Tm	??	3.995	4.71	4.326	4.215	4.88	4.53	4.65	4.17	5.92	6.29	6.36	6.67	5.059	12	6.19	7.65
Yb	??	20.79	24.23	23.21	22.29	25.9	23.51	24.6	21.72	29.4	31.13	32.08	32.31	25.01	60.1	31.1	37.9
Lu	??	2.63	2.983	2.834	2.728	3.32	2.94	3.17	2.751	3.53	3.778	3.856	4.029	2.977	7.3	3.794	4.545

Table 3 REE data and calculated values from apatite trace element concentrations (ppm)

	CBS–12a								CBS–8a							
Sample No	1	2	3	4	5	6	7	8	1	2	3	4	5	6	7	8
LREE	3168.08	3716.67	3477.46	3295.11	4020.1	3614.82	3813.76	3365.92	6257.26	6683.45	6578.63	6830.61	5298.04	11,875.8	6415.56	9034.57
HREE	336.67	389.27	367.96	356.32	400.97	379.95	390.33	355.3	596.54	622.86	626.08	650.4	535.72	1144.5	626.36	801.31
MREE	456.68	528.92	501.45	484.53	544.27	515.46	526.15	483.24	835.24	861.87	870.06	901.45	760.49	1565.8	874.59	1130.1
∑REEs	3504.75	4105.94	3845.42	3651.43	4421.07	3994.77	4204.09	3721.22	6853.8	7306.31	7204.71	7481.01	5833.76	13,020.3	7041.92	9835.88
LREE/HREE	9.41	9.55	9.45	9.25	10.03	9.51	9.77	9.47	10.49	10.73	10.51	10.5	9.89	10.38	10.24	11.27
Zr/Hf	203.7	236.1	370	238.52	215.24	243.13	338.79	309.67	234.03	245.91	313.17	256.62	257.31	222.6	241.25	262.48
Nd/Tb	46.07	46.37	46.1	45.61	47.78	46.69	46.8	46.13	48.83	48.97	49.06	48.3	47.75	48.01	48.7	52.23
La/Sm	3.75	3.77	3.71	3.64	3.98	3.72	3.87	3.67	3.8	3.95	3.84	3.92	3.47	3.84	3.75	4
La/Yb	29.82	29.92	29.08	28.55	30.54	29.35	29.97	29.43	41.26	42.11	40.12	41.57	39.82	38.37	39.87	47.18
Sr/Y	3.11	2.66	2.83	2.92	2.44	2.91	2.77	3.14	1.3	1.1	1.11	0.84	2.06	0.47	1.42	0.64
$(La/Yb)_N$	20.11	20.17	19.61	19.25	20.59	19.79	20.21	19.84	27.82	28.39	27.05	28.02	26.85	25.87	26.88	31.81
Th/U	4.05	4.27	4.18	4.09	4.21	4.17	4.07	4.17	4.05	4.05	4.2	4.2	4.45	5.27	4.17	4.14
Eu/Eu*	0.65	0.65	0.67	0.69	0.67	0.67	0.65	0.68	0.43	0.37	0.4	0.42	0.5	0.36	0.46	0.3
Ce/Ce*	1	1.01	1	1.01	1.03	1.04	1.03	1.04	1.01	1.02	1.02	1.01	1.01	1.02	1.01	1.01

300) excimer laser and a two-volume S155 ablation cell. The experiment was completed in the super purification laboratory. The LA system was coupled to a Neptune Plus MC–ICP–MS (Thermo Fisher, USA). The analysis was performed using a 30 μm-diameter spot at 5 Hz and a fluence of 2 J/cm^2. For every 10–12 analyses of the sample, 91,500 was analyzed twice, and GJ–1 was analyzed once. Typically, 35–40 s of sample signals were acquired after 20 s of gas background measurement. The 91,500 and GJ–1 zircons were used as primary and secondary reference materials, respectively. The exponential function was used for calibrating the downhole fractionation, the Iolite software package was used for data reduction (Paton et al. 2010), and age correction was performed by adopting the method of Sakata et al. (2017). NIST 610 and ^{91}Zr were used to calibrate the trace element concentrations as an external reference material and internal standard element, respectively. The measured ages of the reference materials in the batch were 1063 ± 0.9 Ma, 2σ (91,500) and 604 ± 1.9 Ma, 2σ (GJ-1), which agree well with the reference values within a given uncertainty. The CBS–8 data are listed in Table 6.

Rb–Sr dating of feldspars

Rb–Sr isochron dating of alkaline feldspar and plagioclase in the analysis of basalt was performed at the South Tai Geological Test Institute (STGTI) in Nanjing, China. Before the Rb–Sr isochron dating analysis, we selected fresh test samples with a perfect crystal morphology under a binocular microscope and then accurately measured the contents and isotope ratios of Rb and Sr. The values of ^{87}Rb/^{86}Sr and ^{87}Sr/^{86}Sr were determined by isotope mass spectrometry (VG354, UK). For the detailed experimental analytical process, please refer to Xu et al. 2020. The isotope standard sample was NBS987 (^{87}Sr/^{86}Sr = 0.710236 ± 0.000007), and ^{87}Sr/^{86}Sr = 0.1194 was used for standardization calibration (± 1%, λ(Rb) = 1.42 × 10^{-11} a^{-1}). All operations were carried out in the super purification laboratory, with process blanks for Rb and Sr of 2 × 10^{-10} g and 2 × 10^{-10} g, respectively. The analytical accuracy was better than × 10^{-5}. Isochron ages were calculated according to Brown et al. (1989). The data fitting for the age calculation was performed using Isoplot software by Ludwig (2001). The isochronal regression calculation showed a 2% error for the ^{87}Sr/^{86}Sr ratio and a 0.02% error for the Sr isotope ratio. The data for the alkaline feldspar and plagioclase samples are listed in Table 7.

Results

Summary of the whole–rock geochemistry

In this study, the whole-rock geochemistry of the Naitoushan basalt (CBS–12a) and Heishigou dike (CBS–8a)

Table 4 Contents and isotopic compositions of Sr and Nd for the apatites from CBS–12a and CBS–8a

Sample No	t (Ma)	^{85}Rb (ppm)	^{88}Sr (ppm)	^{144}Nd (ppm)	^{147}Sm (ppm)	^{84}Sr/^{86}Sr	2σ	^{87}Rb/^{86}Sr	2σ	^{87}Sr/^{86}Sr	2σ
CBS–12a–1	0.218	0.00057	1.969	0.29877	0.10360	0.05651	0.00022	0.00091	0.00020	0.70517	0.00021
CBS–12a–2	0.218	0.00061	1.536	0.17201	0.06130	0.05607	0.00040	0.00151	0.00020	0.70534	0.00030
CBS–12a–3	0.218	0.00009	2.009	0.08515	0.03044	0.05667	0.00023	0.00015	0.00004	0.70514	0.00024
CBS–12a–4	0.218	0.00011	1.389	0.10010	0.03555	0.05640	0.00022	0.00024	0.00008	0.70528	0.00026
CBS–12a–5	0.218	0.00014	1.687	0.15810	0.05456	0.05649	0.00033	0.00024	0.00007	0.70485	0.00023
CBS–8a–1	18.7	0.01438	1.542	0.18010	0.06408	0.05627	0.00233	0.03375	0.00665	0.70524	0.00028
CBS–8a–2	18.7	0.00044	2.320	0.16513	0.05780	0.05522	0.00089	0.00082	0.00027	0.70501	0.00023
CBS–8a–3	18.7	0.00122	1.486	0.17796	0.06302	0.05529	0.00057	0.00283	0.00027	0.70482	0.00023
CBS–8a–4	18.7	0.02492	1.947	0.64671	0.22040	0.05562	0.00110	0.03994	0.00406	0.70482	0.00024
CBS–8a–5	18.7	0.00014	1.855	0.22091	0.07773	0.05544	0.00113	0.00026	0.00011	0.70491	0.00026
CBS–12a–1	0.121146	0.000253	0.512613	0.000031	0.70517	0.512613	–0.49	0.351			
CBS–12a–2	0.120435	0.000222	0.512879	0.0000455	0.70534	0.512879	4.70	0.395			
CBS–12a–3	0.120776	0.000256	0.512644	0.0000355	0.70514	0.512644	0.12	0.502			
CBS–12a–4	0.119039	0.000230	0.512400	0.0000325	0.70528	0.512400	–4.64	0.366			
CBS–12a–5	0.1207582	0.000214	0.512651	0.000028	0.70485	0.512651	0.26	0.366			
CBS–8a–1	0.1206222	0.00019	0.512715	0.000036	0.70524	0.512701	1.68	0.302			
CBS–8a–2	0.1232067	0.000226	0.512769	0.0000405	0.70501	0.512754	2.72	0.444			
CBS–8a–3	0.1229755	0.000265	0.512653	0.0000515	0.70482	0.512639	0.46	0.346			
CBS–8a–4	0.120508	0.000322	0.512685	0.0000375	0.70482	0.512671	1.09	0.317			
CBS–8a–5	0.119867	0.000165	0.51273	0.0000375	0.70491	0.512716	1.97	0.273			

was comprehensively reported by Ye et al. (2022) and Li et al. (2021a, b). The Naitoushan basalt (SiO_2 = 50–52 wt%) shows an alkaline affinity and is characterized by high Al_2O_3 and MgO contents, with trace element features similar to those of intraplate basaltic magma. They also have moderately enriched Sr–Nd isotope features, with $(^{87}Sr/^{86}Sr)_i$ = 0.70491–0.70520 and εNd(t) = − 0.9 to − 2.7. The Heishigou dikes (SiO_2 = 48–49 wt%) with OIB affinity are characterized by $Na_2O > K_2O$ and moderately enriched Sr–Nd isotopic signatures ($(^{87}Sr/^{86}Sr)_i$ = 0.70469–0.70450, εNd(t) = − 1.2 to − 1.7). Both have Sr and Nd isotopic compositions similar to those of basalts in the CVF (Li et al. 2021a, b).

Apatite texture

Representative CL images for apatites from CBS–12a and CBS–8a are presented in Fig. 3g and h, respectively. Apatite grains from the Naitoushan basalt (CBS–12a) are euhedral or subhedral and mostly long and columnar in shape (up to 120 μm, Fig. 3g). They commonly occur as inclusions hosted in other major phases, such as plagioclase, indicating that apatite is in an early crystallization phase. Only a few apatite grains have micropores and fractures and are light gray in color.

Apatite grains from the Heishigou dike (CBS–8a) are mostly subhedral crystals (up to 130 μm) and show homogeneous textures (Fig. 3h). They commonly occur as columnar inclusions hosted in plagioclase and phlogopite (Fig. 3f'), with a light gray color in CL images (Fig. 3f' and h).

Chemical composition of apatite

The apatites in Naitoushan basalt (CBS–12a) are low-F magmatic apatites (Fig. 5c; Sun et al. 2021) that have values from 54.13 to 54.28 wt% CaO and 40.22 to 42.87 wt% P_2O_5. They have high K_2O (0.01–0.06 wt%) and MgO (0.15–0.34 wt%) contents and low FeO (0.19–0.35 wt%) contents (Fig. 5a and b; Table 1). The apatites in the Heishigou dike (CBS–8a) have higher F contents and similar CaO and P_2O contents to those in the Naitoushan basalt. Compared to those in the Naitoushan basalt, the Heishigou dike apatites have higher F and lower Al_2O_3 contents. The Cl contents in the apatites of CBS–12a and CBS–8a (Table 1) are equivalent to those in the lunar high-Ti basalts (Ji et al. 2022).

The apatites from CBS–12a and CBS–8a show large ranges for both halogens (Fig. 5c) and Sr contents (566.40–1390.00 ppm) (Fig. 6a; Table 2, Supplementary Tables 1 and 2). The CBS–12a apatites have high Sr (1247.00–1390.00 ppm). As shown in Figs. 6a and 7, Sr shows negative correlations with La, U, ∑REE and La/Yb but a positive correlation with Eu/Eu*. The CBS–12a apatite also has a narrow range of ∑REEs from 3504.75 to 5022.14 ppm (Fig. 7) and is characterized by light REE/heavy REE (LREE/HREE) fractionation (Fig. 6b), with weak negative Eu anomalies (Eu/Eu* = 0.63–0.69).

Table 5 LA–ICP–MS U–Pb apatite data for the Naitoushan basalt (CBS–12) samples from the CTV

Sample No	Total Pb	^{232}Th	^{238}U	Th/U	^{207}Pb/^{206}Pb		^{207}Pb/^{235}U		^{206}Pb/^{238}U		^{207}Pb/^{206}Pb		^{207}Pb/^{235}U		^{206}Pb/^{238}U		^{207}Pb–corrected age (Ma)	±1σ
		ppm	ppm		Ratio	±1σ	Ratio	±1σ	Ratio	±1σ	Age (Ma)	±1σ	Age (Ma)	±1σ	Age (Ma)	±1σ		
CBS–12–1	2.63	61.6	31.6	1.9	0.77592	0.02013	2.62645	0.10608	0.02455	0.00076	4878.2	37	1308.1	29.7	156.3	4.8	20.3	3.9
CBS–12–2	0.86	17.8	3.9	4.6	0.82041	0.0189	6.59252	0.19562	0.05828	0.00109	4957.6	32.8	2058.3	26.2	365.2	6.6	28.3	8.5
CBS–12–3	1.11	17.9	4.0	4.5	0.82195	0.01604	8.25952	0.20516	0.07288	0.00112	4960.3	27.7	2259.9	22.5	453.5	6.7	34.6	9
CBS–12–4	0.90	16.2	3.6	4.6	0.82271	0.01722	7.65575	0.19633	0.06749	0.001	4961.6	29.8	2191.4	23	421	6	31.6	8.9
CBS–12–5	0.91	19.8	4.1	4.8	0.82558	0.01964	6.54528	0.19981	0.0575	0.0011	4966.5	33.8	2052	26.9	360.4	6.7	25.7	8.7
CBS–12–6	0.81	18.2	3.8	4.8	0.82651	0.02287	6.66775	0.24243	0.05851	0.00138	4968.1	39.3	2068.4	32.1	366.6	8.4	25.7	10.3
CBS–12–7	1.15	21.3	4.7	4.5	0.8291	0.0216	6.03019	0.18842	0.05275	0.00091	4972.6	37	1980.2	27.2	331.4	5.6	22.1	8.8
CBS–12–8	0.88	17.3	3.5	5.0	0.82919	0.01565	7.79951	0.21082	0.06822	0.00132	4972.7	26.8	2208.1	24.3	425.4	8	28.6	8.2
CBS–12–9	0.71	14.8	3.1	4.7	0.83051	0.02013	7.05959	0.21453	0.06165	0.00113	4975	34.4	2119	27	385.7	6.9	25.2	9.5
CBS–12–10	0.86	19.1	4.1	4.7	0.83102	0.01841	6.40852	0.18462	0.05593	0.00103	4975.9	31.5	2033.4	25.3	350.8	6.3	22.6	7.9
CBS–12–11	1.03	14.7	3.2	4.6	0.83136	0.0253	9.71242	0.37196	0.08473	0.00197	4976.4	43.2	2407.9	35.3	524.3	11.7	34.1	16.5
CBS–12–12	0.86	15.5	3.5	4.4	0.83144	0.02656	7.70603	0.29016	0.06722	0.00134	4976.6	45.4	2197.3	33.8	419.4	8.1	27	13.7
CBS–12–13	0.81	17.9	3.8	4.8	0.83252	0.02056	6.5211	0.19579	0.05681	0.00097	4978.4	35.1	2048.8	26.4	356.2	5.9	22.3	9
CBS–12–14	0.87	16.7	3.6	4.7	0.83288	0.01979	7.42654	0.22747	0.06467	0.00125	4979	33.8	2164.2	27.4	404	7.6	25.3	9.8
CBS–12–15	1.01	16.6	3.6	4.6	0.83417	0.01819	9.02295	0.28229	0.07845	0.00176	4981.2	31	2340.3	28.6	486.9	10.5	29.9	11
CBS–12–16	1.07	22.0	4.9	4.5	0.8355	0.01901	6.77945	0.1989	0.05885	0.00109	4983.5	32.3	2083	26	368.6	6.6	21.8	8.6
CBS–12–17	0.92	17.8	4.0	4.5	0.83511	0.01986	6.80507	0.21355	0.0591	0.00121	4982.8	33.8	2086.4	27.8	370.1	7.4	22.1	9
CBS–12–18	0.96	19.7	4.3	4.5	0.83668	0.01694	6.88016	0.18689	0.05964	0.00108	4985.5	28.8	2096.1	24.1	373.4	6.6	21.6	7.8
CBS–12–19	0.87	17.8	4.0	4.4	0.83762	0.01947	7.26323	0.22214	0.06289	0.00125	4987.1	33	2144.3	27.3	393.2	7.6	22.3	9.4
CBS–12–20	0.93	21.6	4.6	4.7	0.83818	0.01884	6.10085	0.17423	0.05279	0.00093	4988	31.9	1990.4	24.9	331.6	5.7	18.5	7.7
CBS–12–21	0.92	15.1	3.4	4.5	0.83885	0.0193	8.45942	0.28415	0.07314	0.00179	4989.2	32.7	2281.6	30.5	455	10.8	25.2	10.9
CBS–12–22	0.95	22.5	4.3	5.2	0.84011	0.01787	6.27011	0.17818	0.05413	0.00102	4991.3	30.2	2014.3	24.9	339.8	6.2	18.1	7.4
CBS–12–23	0.91	20.7	4.2	4.9	0.84089	0.02067	6.49159	0.19259	0.05599	0.00093	4992.6	34.9	2044.8	26.1	351.2	5.7	18.4	8.9
CBS–12–24	0.95	19.7	4.2	4.6	0.84176	0.01808	6.97068	0.19378	0.06006	0.00106	4994.1	30.5	2107.7	24.7	376	6.4	19.4	8.4
CBS–12–25	0.89	17.4	3.7	4.7	0.84235	0.01993	7.50982	0.2209	0.06466	0.00113	4995.1	33.6	2174.2	26.4	403.9	6.8	20.6	9.9
CBS–12–26	0.94	15.1	3.3	4.6	0.8427	0.01682	8.56447	0.22356	0.07371	0.00124	4995.7	28.3	2292.8	23.7	458.5	7.4	23.2	9.5
CBS–12–27	0.85	18.2	4.2	4.4	0.84636	0.02178	6.75787	0.23387	0.05791	0.00134	5001.8	36.5	2080.2	30.6	362.9	8.2	16.6	9.7

Table 6 LA–MC–ICP–MS zircon U–Pb data for the Heishigou dike (CBS–8) from the CTV

Sample No	Contents of zircons (ppm)			Th/U	Isotope ratio									^{230}Th disequilibrium corrected age (Ma)	1σ
	Total Pb	^{232}Th	^{238}U		^{207}Pb/^{235}U	1σ	^{206}Pb/^{238}U	1σ	^{238}U/^{206}Pb	1σ	^{207}Pb/^{206}Pb	1σ			
CBS–8–1	0.0141	97.4	140.5	0.7	0.000568	0.000088	0.0000369	0.0000017	27,100.27	1248.522	0.11	0.017	0.325		11.5
CBS–8–2	0.0414	261.2	210	1.2	0.000596	0.000056	0.000042	0.0000014	23,809.52	793.6508	0.105	0.01	0.359		9.2
CBS–8–3	0.2536	1525	748	2.0	0.000613	0.00003	0.00003892	0.00000061	25,693.73	402.7024	0.1156	0.0054	0.336		4.1
CBS–8–4	0.0178	106.1	141.4	0.8	0.00075	0.00012	0.0000418	0.0000021	23,923.44	1201.896	0.137	0.023	0.346		14.5
CBS–8–5	0.0712	482.6	399.6	1.2	0.000533	0.000029	0.00003744	0.00000057	26,709.4	406.6335	0.101	0.0055	0.331		4.0
CBS–8–6	0.02019	120.6	137.8	0.9	0.00074	0.00012	0.0000412	0.0000023	24,271.84	1354.982	0.131	0.022	0.344		15.3
CBS–8–7	0.01395	73.99	91.6	0.8	0.00075	0.00026	0.0000435	0.0000042	22,988.51	2219.58	0.126	0.041	0.360		27.7
CBS–8–8	0.0392	243.98	272.5	0.9	0.000571	0.000048	0.00003952	0.00000095	25,303.64	608.2607	0.106	0.0088	0.343		6.5

Compared with CBS–12a apatites, CBS–8a apatites have low Sr contents (566.40–1193.00 ppm) and a wide range of ∑REE values from 5833.76 to 13,020.30 ppm; they also have high La, Yb, and U contents and La/Yb ratios (38.37–46.17) and strong negative Eu anomalies (Eu/Eu* = 0.34–0.69) (Figs. 7 and 8). The CBS–8a apatites show REE distribution patterns that are similar to those of apatites from CBS–12a (Fig. 6b).

All apatite grains from the studied Naitoushan basalt and Heishigou dike are enriched in light REEs (LREEs) relative to heavy REEs (HREEs), with $(La/Yb)_N$ ratios ranging from 19.20–20.82 and 25.87–31.81, respectively (Table 3 and Supplementary Table 2). In the primitive mantle-normalized trace element and chondrite-normalized REE diagrams (Fig. 6), all apatite grains are enriched in Th, U, and LREEs and depleted in high field strength elements (HFSEs), with strongly negative Rb, Ba, Nb, Ta, K, Zr, Hf and Ti anomalies. They show positive Sr and negative Pb anomalies relative to those of the whole-rock samples of host rocks. Moreover, the CBS–12a and CBS–8a apatite grains have similar Th/U (3.91–5.27), Zr/Hf (165.89–370.00), La/Sm (3.47–4.25) and Nd/Tb (45.59–52.23) ratios, with no correlation with the total REE contents (Fig. 7a, b, c and d).

In situ Sr–Nd isotopic compositions of apatite

The apatite grains of CBS–12a and CBS–8a have highly variable Sr–Nd isotopic compositions (Supplementary Tables 3 and 4); they have relatively high values of ^{143}Nd/^{144}Nd (0.512396–0.512879) and ^{147}Sm/^{144}Nd (0.11127–0.123507) and low ratios of ^{87}Rb/^{86}Sr (0.00015–0.03994) and ^{84}Sr/^{86}Sr (0.05506–0.05720), with no strong relationship with total REE contents (Fig. 7e, f, g and h). CBS–12a apatite grains generally have variable initial ^{87}Sr/^{86}Sr ratios and εNd(t) values of 0.70485–0.70599 and − 4.72 to 4.70, which give an age of 22.2 Ma (Fig. 9a, b and c); these values are significantly distinct from those of CBS–8a apatite grains, which have relatively low initial ^{87}Sr/^{86}Sr ratios (0.70482–0.70533) and positive εNd(t) values (0.46 to 3.80), with an age calculated at 0.218 Ma.

Apatite U–Pb geochronology

The U–Pb data of thirty–two apatite grains from sample CBS–12 (Supplementary Tables 4 and 5) plotted on a Tera–Wasserburg diagram (Fig. 4a) show discordant ages with rather high proportions of common Pb and ^{207}Pb/^{206}Pb ratios between 0.77 and 0.85. They yield a lower intercept age of 18.7 ± 2.6 Ma with an initial ^{207}Pb/^{206}Pb value of 0.8837 (Fig. 4a). The weighted average ^{207}Pb-corrected ages are consistent at 22.2 ± 2.9 Ma (Fig. 4b).

Table 7 Rb–Sr dating results for alkaline feldspar and plagioclase from CBS–8

Sample No	Mineral	Rb (ppm)	Sr (ppm)	$^{87}Rb/^{86}Sr$	error	$^{87}Sr/^{86}Sr$	error	$(^{87}Sr/^{86}Sr)_i$
CBS–8–1	Plagioclase	115.3	10.15	33.47	0.01	0.703671	0.00005	0.70357
CBS–8–2	Plagioclase	121.6	16.28	21.96	0.01	0.703605	0.00005	0.70354
CBS–8–3	Plagioclase	73.87	3.892	56.06	0.01	0.703746	0.00005	0.70357
CBS–8–4	Plagioclase	76.85	4.472	50.69	0.01	0.703705	0.00005	0.70355
CBS–8–5	Plagioclase	15.27	449.6	0.1023	0.01	0.703615	0.00005	0.70361
CBS–8–6	Plagioclase	12.89	397.2	0.0954	0.01	0.703583	0.00005	0.70358
CBS–8–7	K-feldspar	210.3	2.139	290.2	0.01	0.704466	0.00005	0.70357
CBS–8–8	K-feldspar	227.8	2.269	295.3	0.01	0.704469	0.00005	0.70355

Zircon U–Pb dating

Zircons from the Heishigou dike (CBS–8) are light gray with few inclusions. They are euhedral columnar crystals with sizes of 55–180 μm. They exhibit homogeneous luminescence and occasionally display oscillatory zoning (Fig. 4c). Th/U ratios range from 0.7 to 2.0, and the zircons have a magmatic origin (Hoskin and Schaltegger 2003). The 8 analyses of zircons from CBS–8 provide ^{230}Th disequilibrium-corrected ages of 0.325–0.360 Ma (Table 6). Tera–Wasserburg concordia diagrams are used to calculate the lower intersection age (0.2301 ± 0.0049 Ma, Fig. 4c).

Rb–Sr dating of alkaline feldspar and plagioclase

The Rb and Sr concentrations and isotopic compositions from alkaline feldspars and plagioclases in the eight CBS–8 samples are presented in Table 7. All analyzed samples have relatively low Rb and Sr contents of 12.89–227.8 ppm and 2.139–449.6 ppm, respectively. The $^{87}Rb/^{86}Sr$ ratios

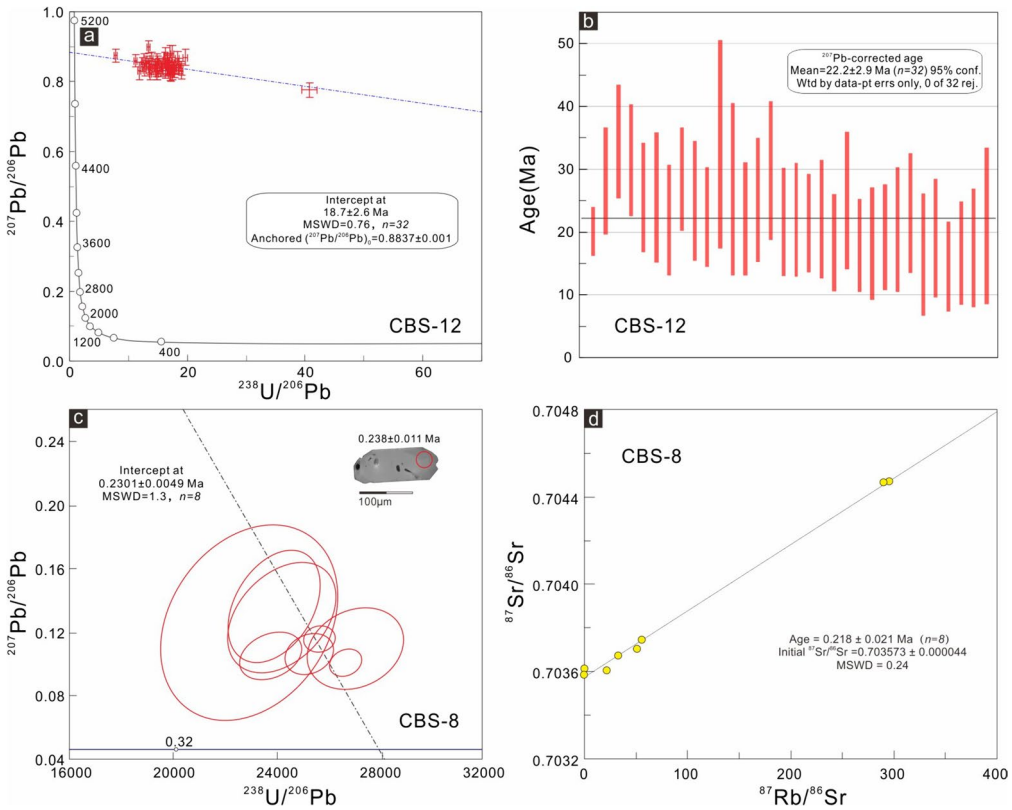

Fig. 4 **a** Tera–Wasserburg concordia and **b** weighted average ^{207}Pb-corrected age plots for LA–ICP–MS U–Pb apatite analyses from the Naitoushan basalt. **c** Tera–Wasserburg concordia age plot for LA–MC–ICP–MS U–Pb zircon analyses from the Heishigou dike. **d** Rb–Sr isochron age diagram for alkaline feldspar and plagioclase from the Heishigou dike

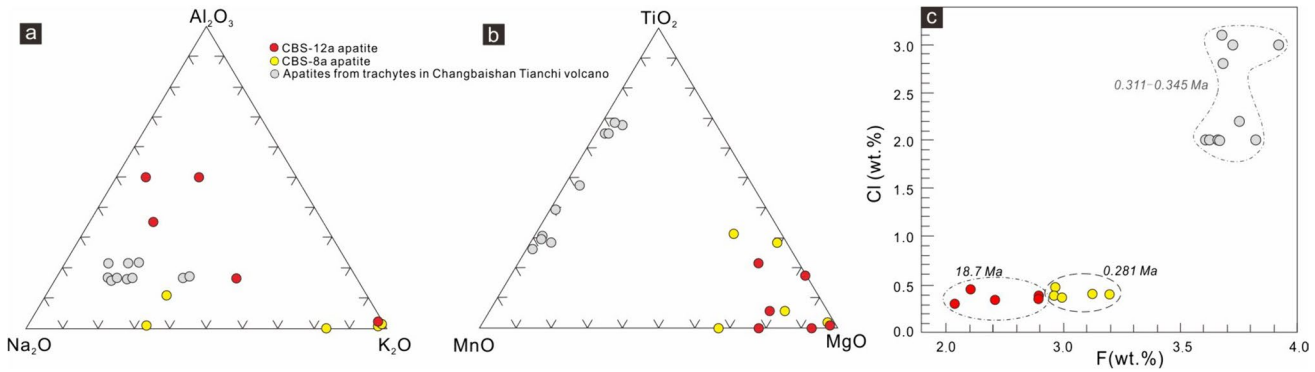

Fig. 5 **a** Al_2O_3–Na_2O–K_2O, **b** TiO_2–MnO–MgO and **c** Cl–F diagrams for the apatite samples from the Naitoushan basalt and Heishigou dike. Other data for apatites from trachytes in the CVF are from Wei (2014)

vary from 0.0954 to 295.3, the $(^{87}Sr/^{86}Sr)_i$ values range from 0.70354 to 0.70361, and the initial $^{87}Sr/^{86}Sr$ ratio is 0.703573 ± 0.000044. In the $^{87}Rb/^{86}Sr$ vs. $^{87}Sr/^{86}Sr$ diagram (Fig. 4d), the data yield a Rb–Sr isochron age of 0.218 ± 0.021 Ma (mean standard weighted deviation (MSWD) = 0.24, n = 8).

Discussion

Ages of the Naitoushan basalt and Heishigou dike

All the apatite grains from the Naitoushan basalt and Heishigou dike are euhedral or subhedral, and most are long and columnar in shape (Fig. 3g and h). Their Th/U ratios range from 1.9–5.2, indicating a magmatic origin. Compared with the previously published age of the Naitoushan basalt (K – Ar age of 13 – 16 Ma, alkaline feldspars; Liu 1988), our LA–ICP–MS U–Pb age for apatite is considerably more accurate because apatite has a low crystallization temperature that represents the final cooling age of the magma (Chew et al. 2014). The apatite U–Pb analyses yield an age of 18.7 ± 2.9 Ma for the lower intercept (n = 32, Fig. 4a) and a weighted mean ^{207}Pb-corrected age of 22.2 ± 2.9 Ma for CBS–12a (Fig. 4b), implying that the large-scale eruption of magma occurred in the Miocene Aquitanian stage (22.2 Ma) and that the final cooling time of the magma occurred in the Burdigalian stage (18.7 Ma). All dated zircons from the Heishigou dike (CBS–8a) are euhedral columnar crystals and display oscillatory zoning, and their Th/U

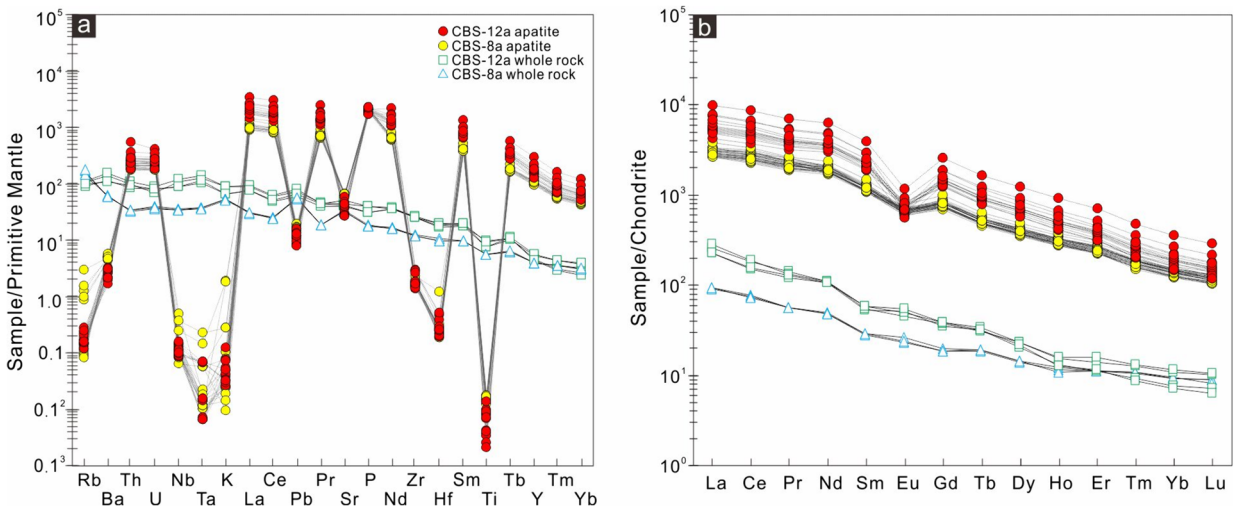

Fig. 6 **a** Primitive mantle-normalized trace element patterns and **b** chondrite-normalized REE patterns (McDonough and Sun 1995) for CBS–12a and CBS–8a apatite grains and host rocks. Other whole-rock data are from Yan et al. (2023)

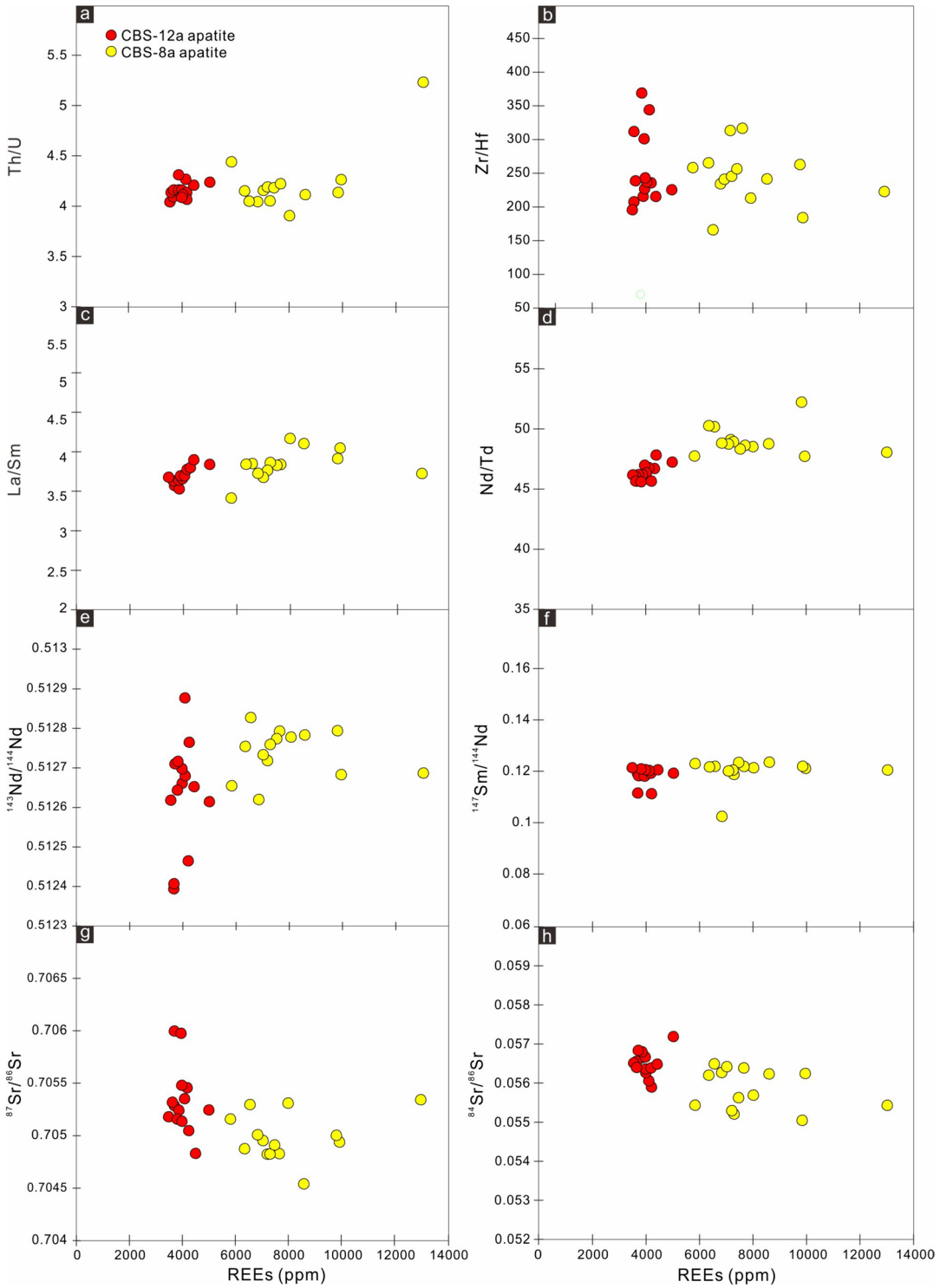

Fig. 7 Plots of **a** La, **b** Yb, **c** REEs, **d** La/Yb, **e** Eu/Eu*, and **f** U vs. Sr contents for the apatite grains from CBS–12a and CBS–8a

ratios range from 0.7 to 2.0, implying a magmatic origin. The single-grain LA–MC–ICP–MS zircon U–Pb intercept age is 0.2301 ± 0.0049 Ma (n = 8; Fig. 4c). Our data for alkaline feldspar and plagioclase Rb–Sr isochron ages of 0.218 ± 0.021 Ma (n = 8; Fig. 4d) correspond well with the emplacement age of the zircon; thus, we conclude that the studied Heishigou dike was emplaced in the Chibanian stage of the Pleistocene. The age of CBS–12a is definitely older

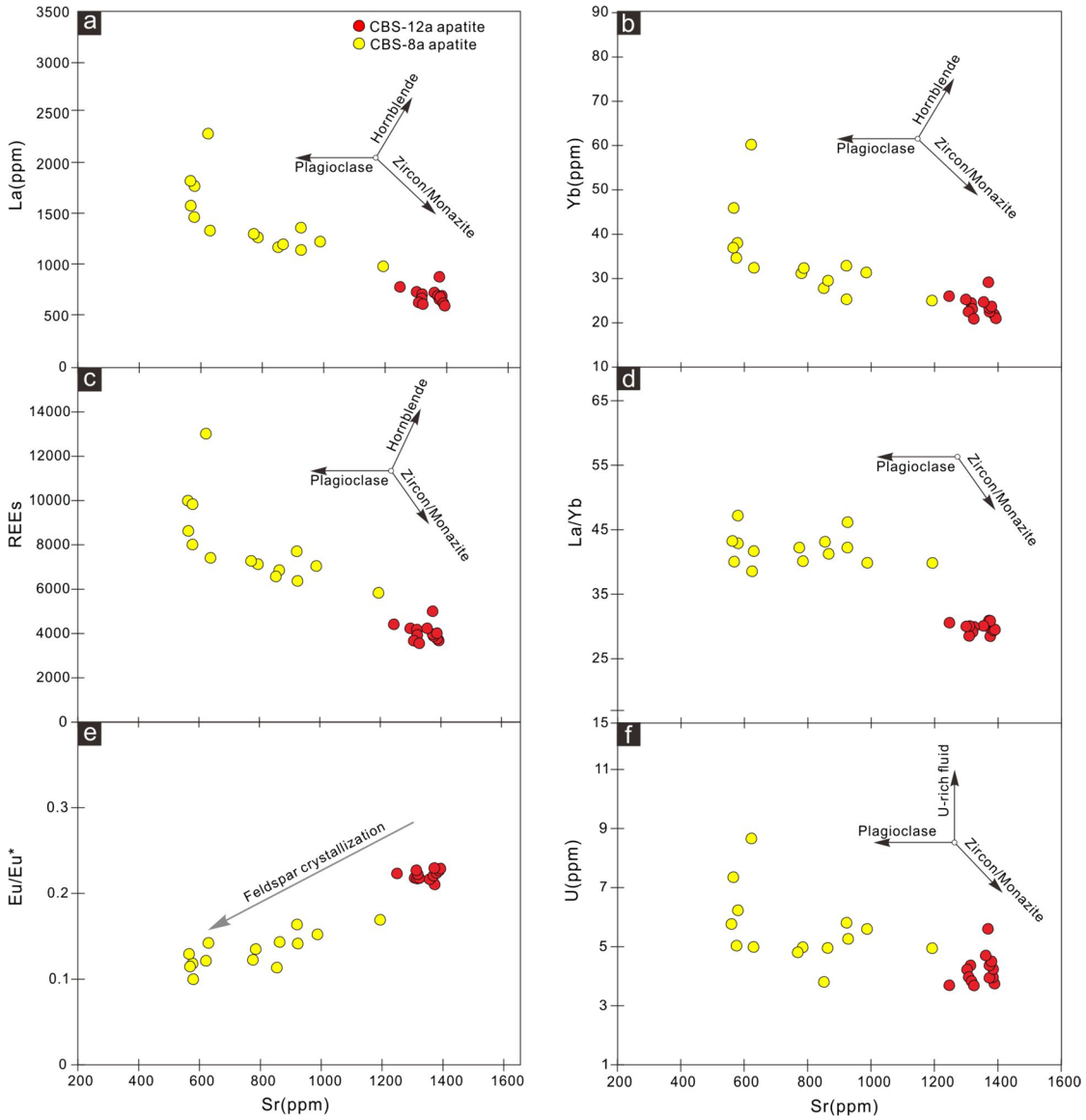

Fig. 8 Plots of **a** Th/U, **b** Zr/Hf, **c** La/Sm, **d** Nd/Td, **e** $^{143}Nd/^{144}Nd$, **f** $^{147}Sm/^{144}Nd$, **g** $^{87}Sr/^{86}Sr$, and **h** initial $^{84}Sr/^{86}Sr$ ratios vs. REE values for the apatite grains from CBS–12a and CBS–8a

than the age of CBS–8a, indicating that the Heishigou dike was emplaced after the Naitoushan basalt. This conclusion is consistent with the geological relationships because the Heishigou dike intruded the earlier and larger irregular Naitoushan basalt (Fig. 2).

As previously reported, the last three main stages of CTV volcanism are the shield stage (2.8 to 0.3 Ma), cone construction stage (1.5 to 0.01 Ma), and caldera-forming stage (0.2 Ma to present). The preshield stage mainly resulted in Gaima Plateau basalts (such as the Naitoushan basalt). Therefore, our new geochronological data also show that the Heishigou dike was emplaced before the pre-shield/shield/cone-forming stage. Furthermore, the NE–SW strike of the Heishigou dike also reveals the structural discontinuity affecting the CTV, i.e., the Tianchi–Zengfengshan fault, and the preferred alignment of the scoria cones (Figs. 1c and 2).

Origin of apatite from the Naitoushan basalt and Heishigou dike

CBS–12a apatite is in a late crystallization phase in the Naitoushan basalt; it occurs as euhedral or subhedral grains between plagioclase grains. This apatite generally displays higher Sr and lower Cl concentrations and shows negative correlations with La, Yb, U, REEs, La/Yb and Eu/Eu* (Fig. 8a, b, c, d, e and f), indicating simultaneous

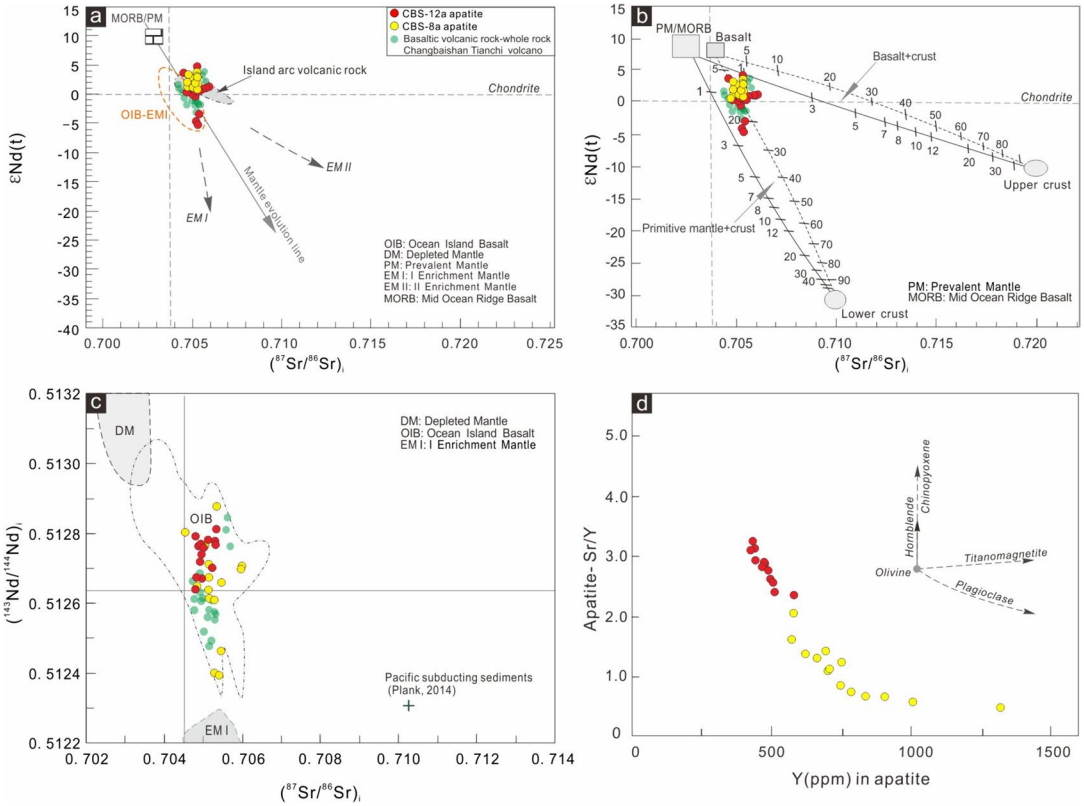

Fig. 9 **a** and **b** Plots of εNd(t) vs. $(^{87}Sr/^{86}Sr)_i$ for apatite grains from CBS–12a and CBS–8a (Sun et al. 2014). **c** $(^{143}Nd/^{144}Nd)_i$ vs. $(^{87}Sr/^{86}Sr)_i$ plot of apatite grains and volcanic basalts from the CVF (Zhang et al. 2018). **d** Sr/Y vs. Y plot of apatites (Sun et al. 2022)

plagioclase, zircon and monazite accumulation during magmatic evolution (Zhang et al. 2019; Kendrick et al. 2014). Our previous study based on whole-rock Sr–Nd–Pb isotopes indicated that the magma with OIB attributes played an insignificant role in the formation of the Naitoushan basalt (Li et al. 2021a, b). Accordingly, the variations in the Th/U (4.05–4.31), Zr/Hf (191.93–370.00), La/Sm (3.59–3.98), Nd/Tb (45.59–47.78), $^{143}Nd/^{144}Nd$ (0.512396–0.512879), and $^{147}Sm/^{144}Nd$ (0.11127–0.121146) ratios in CBS–12a apatite are small, indicating limited crustal contamination of the parental magma. The ratio of Sr isotopes in apatite can better reflect the non-contaminated original initial magma (such as by alteration or source variation), or they can indicate a lower degree of contamination than shown by whole-rock geochemistry (Charlier et al. 2006). For CBS–12a, the $^{87}Sr/^{86}Sr$ (0.70485–0.70599) and $^{84}Sr/^{86}Sr$ (0.05591–0.05720) ratios are lower than those of the whole-rock samples (Fig. 9a, b, and c), indicating that these apatites were produced through fractional crystallization of magma.

The negative relationships of U, La, Yb, REEs, La/Yb and Sr in the CBS–12a apatite indicate that olivine + pyroxene + plagioclase ± monazite ± zircon-dominated fractionation contributed to magmatic evolution (Pan et al. 2016; Fig. 8a, b, c, d and f). The Eu/Eu* values in the CBS–12a apatite increased with increasing Sr (Fig. 8e), reflecting the influence of fractional crystallization of feldspar (Ladenburger et al. 2016). The experimental results also showed that the partition coefficients of REEs between apatite and melt were easily affected by the composition of the magma, i.e., an increase in the SiO_2 content (Prowatke and Klemme 2006). In a magmatic system, feldspar fractionation could lead to decreasing Sr and increasing SiO_2 and REEs during the magmatic evolutionary process, thereby increasing the partition coefficients of REEs. Correspondingly, apatite crystallizing from the magma could contain high ∑REEs (Fig. 6b) and low Sr contents (Fig. 6a). The CBS–12a apatites have lower ∑REE contents and Sr/Y values and higher Sr/Y and lower Y ratios than those from CBS–8a (Figs. 7, 8 and 9d), indicating that the basaltic magma underwent fractional crystallization to a limited degree (Sun et al. 2022). The results also reveal significant decreases in La, Yb and La/Yb with Sr but increases in F/Cl (Fig. 5c), Th/U, Zr/Hf, La/Sm and Nd/Tb with REEs (Fig. 7a, b, c and d), which is consistent with feldspar fractionation (Zhang et al. 2020).

The CBS–8a apatites have Th/U (3.91–5.27), Zr/Hf (165.89–316.51), La/Sm (3.47–4.25), Nd/Tb (47.73–52.23), $^{143}Nd/^{144}Nd$ (0.512653–0.512824), $^{147}Sm/^{144}Nd$ (0.119867–0.123507), $^{87}Sr/^{86}Sr$ (0.70482–0.70533) and

$^{84}Sr/^{86}Sr$ (0.05506–0.05649) ratios and almost identical $(^{87}Sr/^{86}Sr)_i$ (0.70482–0.70533) and εNd(t) (0.46–3.80) values to those of the OIB–EMI (Armienti and Gasperini 2007) (Fig. 9a, b and c), further indicating a weak fractional crystallization relationship between the Heishigou dike and the Naitoushan basalts with increasing REEs. According to the primitive mantle-normalized trace element patterns and chondrite-normalized REE patterns, the whole-rock composition of CBS–8a has the same trend and is slightly lower than that of the Naitoushan basalt, suggesting that the Heishigou dike and Naitoushan basalt may have originated from the same magma with a continuous weak fractional crystallization process; this interpretation is also supported by the right-leaning distribution of rare earth elements (Yan et al. 2023), as shown in Fig. 6. The volume of Heishigou dike rocks in outcrop is quite small relative to that of the Naitoushan basalt (Fig. 2), which is also consistent with a fractionation model, where the mafic magma generally has a much smaller dike volume than basalt (Chandrasekharam et al. 2000; Petcovic and Grunder 2003). The continuous compositional variations in apatite between the Heishigou dike and the Naitoushan basalt (Figs. 6, 7, 8 and 9d) are also consistent with the trends defined by weak fractional crystallization. In general, CBS–8a apatites show a closer affinity to CBS–12a apatites, indicating their similar origin. The CBS–8a apatites show lower Al_2O_3 and MgO contents and higher F contents (Fig. 5); these features are potentially attributed to fractionation of Al-, Mg- and F-bearing minerals, such as clinopyroxene and olivine (Aoki et al. 1981; Busa et al. 2002; Beyer et al. 2012). Alternatively, the relationships of Sr with La, Yb, REEs, U and La/Yb indicate simultaneous crystallization of other REE- and U-rich minerals, accompanied by the formation of apatite. Generally, plagioclase in magma generally has a high Sr content and low element diffusion rate (Costa et al. 2003), so the Sr isotope ratios in the analyzed apatite can reflect mineral crystallization in the parental magma, and the $^{87}Sr/^{86}Sr$ and $^{84}Sr/^{86}Sr$ values in apatite (Fig. 8g and h) slightly decrease with increasing REEs in response to feldspar fractionation during magmatic evolution (Belousova et al. 2001; Bruand et al. 2017). To produce the whole-rock geochemical results of the Heishigou dike and the trace element and Nd isotopic compositions of apatite, the Heishigou dike is likely derived from an enriched mantle with εNd(t) values (Fig. 9a, b and c) similar to those of the Naitoushan basalt.

Implications for the petrogenesis of basalts

Apatite grains in the host basalts have similar occurrences, geochemical features, and Sr–Nd isotopic compositions, indicating that they have the same origins. The apatites of the Naitoushan basalt (CBS–12a) crystallized from magma under equilibrium or near-equilibrium conditions, with no other late crystallization phases (Webster and Piccoli 2015). They have narrow initial $^{87}Sr/^{86}Sr$ and $^{143}Nd/^{144}Nd$ ratios (0.70485–0.70599 and 0.512396–0.512879, respectively) and variable εNd(t) values (−4.72 to 4.70), and their Sr–Nd isotopic compositions are similar to those of host basalts (Fig. 9a, b and c; Ye et al. 2022), indicating that these apatites crystallized from the host magma. The apatites from the Heishigou dike (CBS–8a) have relatively variable $(^{87}Sr/^{86}Sr)_i$ and $(^{143}Nd/^{144}Nd)_i$ ratios (0.70482–0.70533 and 0.512639–0.512810, respectively) and εNd(t) values (0.46–3.80) and an age of 0.218 Ma. Their Sr–Nd isotopic compositions are generally similar to those of the host magmatic apatite grains of the Heishigou dike and Naitoushan basalt (Supplementary Tables 3 and 4), indicating that they potentially crystallized from the same magma source. Furthermore, apatite can also be inherited from source materials, thus providing insight into the origins of magma or petrogenesis (Watson and Green 1981; Wolf and London 1994; Dempster et al. 2003). The Sr–Nd isotopic compositions of the CBS–12a and CBS–8a apatites, which are similar to those of the host Naitoushan basalt and Heishigou dikes, agree with an inherited origin of the Rb–Sr and Sm–Nd isotope systematics of magmatic melt (Chappell et al. 1987; White et al. 1999). Therefore, we infer that the CBS–12a and CBS–8a apatite grains may represent host magma originating from a possibly depleted mantle source but modified by crustal contamination or the involvement of enriched components in the source.

Bruand et al. (2020) and Piccoli and Candela (2002) suggested that accessory minerals not only affect the trace element chemistry of host rocks but also record changes in the magmatic composition during magmatic evolution, i.e., magmatic differentiation. The relatively narrow range of initial $^{87}Sr/^{86}Sr$ ratios and εNd(t) values (Fig. 9a, b and c) in the CBS–12a and CBS–8a apatites indicates that there was limited crustal assimilation and that no subducted sedimentary material was involved in the genesis of apatite. Apatites from CBS–12a and CBS–8a display strong correlations between Th/U, Zr/Hf, La/Sm, Nd/Tb, $^{143}Nd/^{144}Nd$, $^{147}Sm/^{144}Nd$, $^{87}Sr/^{86}Sr$, $^{84}Sr/^{86}Sr$ and REE contents (Fig. 7); these characteristics of magmatic apatite are attributed to the crystallization of minerals, with progressive depletion of the remaining magmatic melt in trace elements (Miles et al. 2013). The most striking geochemical features of apatites in CBS–12a and CBS–8a that crystallized from magma are their variable Sr anomalies (Fig. 8), with contents ranging from 1390.00 to 566.40 ppm. The Sr content is generally controlled by various factors, such as the crystallization of feldspars or the oxidation state of the host magma (Ramos et al. 2004; Yuan et al. 2018). For variable oxidation states, Ce and Eu are usually presumed to exist in large quantities in apatite (Piccoli and Candela 2002); however, correlations between Ce or Eu anomalies and the oxidation state of their host magmas have not been reported. There are no significant Ce anomalies (Ce/Ce* = 1.06–1.00, in apatite,

Supplementary Tables 4 and 5) and no MnO content variations (~0.7 wt%; Table 1) in the apatites from CBS–12a and CBS–8a. The crystallization of plagioclase effectively reduces Sr and Eu contents from magma (Ching–Oh et al. 1974), and the Sr contents and Eu anomalies decrease with increasing amounts of plagioclase (Figs. 6 and 7). The apatites in CBS–12a and CBS–8a that crystallized from the host magma have variable medium REE (MREE) contents (1157.56–456.68), with Nd/Tb ratios weakly increasing with increasing REE contents (Fig. 7d). Titanite and zircon have high mineral/melt partition coefficients for MREEs (Sm + Eu + Gd + Tb + Dy; Sun et al. 2022), and during crystallization, they are also enriched in U; thus, their crystallization in host basaltic magmas can potentially explain the increasing Nd/Tb ratios of apatites.

Apatites in CBS–12a and CBS–8a have decreasing Th, U and REE contents and Sr/Y ratios; weakly increasing Th/U, La/Sm and Nd/Tb ratios; and relatively uniform Zr/Hf and Sr–Nd isotope ratios (Figs. 6, 7 and 8). Therefore, these results can potentially indicate coeval crystallization of titanite and other minerals, such as feldspar and monazite (Bingen et al. 1996; Lloyd et al. 1996; Bruand et al. 2016), and depletions in Hf, Zr, Nb, and Ta (Fig. 6a) can potentially be caused by the cocrystallization of zircon (Nardi et al. 2013). This interpretation is also consistent with the petrographic characteristics of euhedral–subhedral apatites enclosed in plagioclase (Fig. 3e, f and f'). Their variations in Eu anomalies (0.69–0.34) are attributed to weak plagioclase crystallization or fractionation in the magma chamber, with an EMI-type nature. Furthermore, the whole-rock apatite samples from the Naitoushan basalt and Heishigou dikes have relatively high REE and trace element contents (Fig. 6b) and relatively evident negative Eu anomalies, further indicating fractional crystallization of feldspars and accessory minerals. In addition, a slab of the Pacific plate in the MTZ (mantle transition zone) and a large mantle wedge (BMW) below NE China have been confirmed by seismic imaging data (Tian et al. 2016). Beginning in the middle Cenozoic, the subducted plate gradually subsided into the MTZ, resulting in water-rich melt, and slab-derived fluids may have metasomatized the overlying mantle (Li et al. 2021a, b). Combined with the geochemistry of the gas emitted in NE China (Xu et al. 2013) and of the Cenozoic basalts on the continental margin of NE China (Zhang et al. 2009), the EM1 source magma could have originated in the subcontinental lithospheric mantle (SCLM), so the EMI signature of the studied dikes and basalts in the CVF can be explained by the back-arc extension and rifting caused by the rollback of the Pacific plate (Kuritani et al. 2009; Zheng et al. 2018). The tomography data in NE China (Zhu et al. 2019) also clearly show a thickening of the Moho due to the accumulation of mantle melts at the base of the crust below the CVF. Therefore, we propose that the dikes and basalts in the CVF occur at the Moho depth.

Based on these results, these crystal features of minerals, geochemical and isotopic characteristics of apatites and whole-rock compositions of the Naitoushan basalt and Heishigou dike represent a continuous phase that crystallized from mafic magmas that came from a magma source with OIB–EMI affinity.

Conclusions

Based on the integrated in situ oxide, volatile element and Sr–Nd isotope analyses of apatite and geochronology of the Naitoushan basalt and Heishigou dikes from the CTV, the following conclusions can be drawn:

1. The ages of the Naitoushan basalt and Heishigou dike in the Changbaishan area are 22.2 ~ 18.7 Ma and 0.231 ~ 0.218 Ma, respectively. This indicates that the basaltic magmatism between the preshield and postshield stages of the CTV potentially lasted for 22 Ma until the cone formation stage.
2. The apatites from the Naitoushan basalt and Heishigou dike are characterized by low FeO, MnO, TiO2, F, and Cl contents and high MgO and K2O + Na2O concentrations, indicating their crystallization from alkaline mafic host magmas with limited volatile contents.
3. The chemical and Sr–Nd isotopic compositions from whole-rock and apatite samples of the Naitoushan basalt and Heishigou dike collectively indicate that the preshield and postshield magmas were derived from an enriched mantle source with EMI-type attributes, related to the rollback of the Pacific plate. The host magmas of apatites were controlled mainly by weak crystallization of olivine, pyroxene, plagioclase, and other cocrystallizing accessory minerals.

Supplementary Information The online version contains supplementary material available at https://doi.org/10.1007/s00710-024-00863-4.

Acknowledgements We are grateful to the Editor in Chief and the anonymous reviewers for their constructive comments and suggestions, which have substantially improved the presentation of this paper. This research was financially supported by the National Nonprofit Fundamental Research Grant of China, Institute of Geology, China Earthquake Administration (NORSCBS22–05 and NORSCBS22–06) and the China Scholarship Council (202104190014).

References

Aleinikoff JN, Lund K, Fanning CM (2015) SHRIMP U-Pb and REE data pertaining to the origins of xenotime in Belt Supergroup rocks: evidence for ages of deposition, hydrothermal alteration, and metamorphism. Can J Earth Sci 52(9):722–745

Aoki K, Ishiwaka K, Kanisawa S (1981) Fluorine geochemistry of basaltic rocks from continental and oceanic regions and petrogenetic application. Contrib Mineral Petrol 76:53–59

Armienti P, Gasperini D (2007) Do we really need mantle components to define mantle composition? J Petrol 48(4):693–709

Barfod GH, Krogstad EJ, Frei R, AlbarÃ¨de, F. (2005) Lu-Hf and PbSL geochronology of apatites from Proterozoic terranes: A first look at Lu-Hf isotopic closure in metamorphic apatite. Geochim Cosmochim Ac 69(7):1847–1859

Basu AR, Wang JW, Huang WK, Xie GH, Tatsumoto M (1991) Major element, REE, and Pb, Nd and Sr isotopic geochemistry of Cenozoic volcanic rocks of eastern China: implications for their origin from suboceanic-type mantle reservoirs. Earth Planet Sci Lett 105(1–3):149–169

Belousova EA, Walters S, Griffin WL, O'reilly SY (2001) Trace-element signatures of apatites in granitoids from the Mt Isa Inlier, northwestern Queensland. Aust J Earth Sci 48(4):603–619

Beyer C, Klemme S, Wiedenbeck M, Stracke A, Vollmer C (2012) Fluorine in nominally fluorine-free mantle minerals: Experimental partitioning of F between olivine, orthopyroxene and silicate melts with implications for magmatic processes. Earth Planet Sci Lett 337–338:1–9

Bingen B, Demaiffe D, Hertogen J (1996) Redistribution of rare earth elements, thorium, and uranium over accessory minerals in the course of amphibolite to granulite facies metamorphism: The role of apatite and monazite in orthogneisses from southwestern Norway. Geochim Cosmochim Ac 60(8):1341–1354

Broom-Fendley S, Brady AE, Wall F, Gunn G, Dawes W (2017) REE minerals at the Songwe Hill carbonatite, Malawi: HREE-enrichment in late-stage apatite. Ore Geol Rev 81:23–41

Brown RW, Allsoppl HL, Bristow JW, Smith CB (1989) Improved precision of Rb–Sr dating of kimberlitic micas: An assessment of a leaching technique. Chem Geol 79(2):125–136

Bruand E, Fowler M, Storey C, Darling J (2017) Apatite trace element and isotope applications to petrogenesis and provenance. Am Mineral 102(1–2):75–84

Bruand E, Fowler M, Storey C, Laurent O, Nebel O (2020) Accessory mineral constraints on crustal evolution: elemental fingerprints for magma discrimination. Geochem Perspect Lett 13:7–12

Bruand E, Storey C, Fowler M (2016) An apatite for progress: Inclusions in zircon and titanite constrain petrogenesis and provenance. Geology 44(2):91–94

Busa T, Clochiatti R, Cristofolini R (2002) The role of apatite fractionation and REE distribution in alkaline rocks from Mt. Etna. Sicily Miner Petrol 74:95–114

Cao MJ, Zhou QF, Qin KZ, Tang DM, Evans NJ (2013) The tetrad effect and geochemistry of apatite from the Altay Koktokay No. 3 pegmatite, Xinjiang, China: implications for pegmatite petrogenesis. Miner Petrol 107:985–1005

Chandrasekharam D, Vaselli O, Sheth HC, Keshav S (2000) Petrogenetic significance of ferro-enstatite orthopyroxene in basaltic dikes from the Tapi rift, Deccan flood basalt province, India. Earth Planet Sci Lett 179(3–4):469–476

Chappell BW, White AJR, Wyborn D (1987) The importance of residual source material (restite) in granite petrogenesis. J Petrol 28(6):1111–1138

Charlier BLA, Ginibre C, Morgan D, Nowell GM, Pearson DG, Davidson JP, Ottley CJ (2006) Methods for the microsampling and high-precision analysis of strontium and rubidium isotopes at single crystal scale for petrological and geochronological applications. Chem Geol 232(3–4):114–133

Chen H, Xia QK, Ingrin J, Deloule E, Bi Y (2017) Heterogeneous source components of intraplate basalts from NE China induced by the ongoing Pacific slab subduction. Earth Planet Sci Lett 459:208–220

Chen SS, Lee SG, Simutė S, Fichtner A, Lee TJ, Lee YS, Liu JQ, Gao R (2021) Geochemical and seismic tomography constraints of two-layer magma chambers beneath the bimodal volcanism: A case study of late Cenozoic volcanic rocks from Ulleung Island and Mt. Changbai (Paektu). Chem Geol 581:120386

Chen Y, Zhang YX, Graham D, Su SG, Deng JF (2007) Geochemistry of cenozoic basalts and mantle xenoliths in Northeast China. Lithos 96(1–2):108–126

Cherniak DJ (2005) Uranium and manganese diffusion in apatite. Chem Geol 219(1–4):297–308

Chew DM, Petrus JA, Kamber BS (2014) U-Pb LA-ICP-MS dating using accessory mineral standards with variable common Pb. Chem Geol 363(3):185–199

Ching-oh S, Williams RJ, Shine-soon S (1974) Distribution coefficients of Eu and Sr for plagioclase-liquid and clinopyroxene-liquid equilibria in oceanic ridge basalt: an experimental study. Geochim Cosmochim Acta 38(9):1415–1433

Choi HO, Choi SH, Lee YS, Ryu JS, Lee DC, Lee SG, Sohn YK, Liu JQ (2020) Petrogenesis and mantle source characteristics of the late Cenozoic Baekdusan (Changbaishan) basalts, North China Craton. Gondwana Res 78:156–171

Choi HO, Choi SH, Yu Y (2014) Isotope geochemistry of Jeongok basalts, northernmost South Korea: Implications for the enriched mantle end-member component. J Asian Earth Sci 91:56–68

Chu MF, Wang KL, Griffin WL, Chung SL, O'Reilly SY, Pearson NJ, Iizuka Y (2009) Apatite composition: Tracing petrogenetic processes in Transhimalayan granitoids. J Petrol 50(10):1829–1855

Cochrane R, Spikings RA, Chew D, Wotzlaw J-F, Chiaradia M, Tyrrell S, Schaltegger U, Van der Lelij R (2014) High temperature (>350 °C) thermochronology and mechanisms of Pb loss in apatite. Geochim Cosmochim Ac 127:39–56

Costa F, Chakraborty S, Dohmen R (2003) Diffusion coupling between trace and major elements and a model for calculation of magma residence times using plagioclase. Geochimica Et Cosmochimica Ac 67(12):2189–2200

Dempster TJ, Jolivet M, Tubrett MN, Braithwaite CJR (2003) Magmatic zoning in apatite: a monitor of porosity and permeability change in granites. Contrib Mineral Petr 145(5):568–577

Dong Y, Xiong S, Wang F, Ji Z, Li YB, Yamamoto S, Niida K, Xu WL (2023) Triggering of episodic back-arc extensions in the northeast Asian continental margin by deep mantle flow. Geology 51(2):193–198

Donovan JJ, Tingle TN (1996) An improved mean atomic number background correction for quantitative microanalysis. Microsc Microanal 2(1):1–7

Gilder SA, Keller GR, Luo M, Goodell PC (1991) Eastern Asia and the Western Pacific timing and spatial distribution of rifting in China. Tectonophysics 197(2–4):225–243

Hoskin PWO, Schaltegger U (2003) The composition of zircon and igneous and metamorphic petrogenesis. Rev Mineral Geochem 53(1):27–62

Ji JL, He HC, Hu S et al (2022) Magmatic chlorine isotope fractionation recorded in apatite from Chang'e-5 basalts. Earth Planet Sci Lett 591:117636

Jochum KP, Stoll B, Herwig K et al (2006) MPI-DING reference glasses for in situ microanalysis: New reference values for element concentrations and isotope ratios. Geochem Geophys Geosyst 7(2):217–222

Kendrick MA, Jackson MG, Kent AJ, Hauri EH, Wallace PJ, Woodhead J (2014) Contrasting behaviours of CO_2, S, H_2O and halogens (F, Cl, Br, and I) in enriched-mantle melts from Pitcairn and Society seamounts. Chem Geol 370:69–81

Kuritani T, Kimura JI, Miyamoto T, Wei H, Shimano T, Maeno F, Xu J, Tan GC (2009) Intraplate magmatism related to deceleration of up welling asthenospheric mantle: Implications from the Changbaishan shield basalts, Northeast China. Lithos 112:247–258

Ladenburger S, Marks MA, Upton B, Hill P, Wenzel T, Markl G (2016) Compositional variation of apatite from rift–related alkaline

igneous rocks of the Gardar Province, South Greenland. Am Mineral 101(3):612–626

Laurent O, Zeh A, Gerdes A, Villaros A, Gros K, Słaby E (2017) How do granitoid magmas mix with each other? Insights from textures, trace element and Sr-Nd isotopic composition of apatite and titanite from the Matok pluton (South Africa). Contrib Mineral Petr 172(9):1–22

Lee SH, Oh CW, Lee YS, Lee SG, Liu JQ (2021) Petrogenesis of the Cenozoic volcanic rocks in Baekdu volcano in northeastern Asia and the expected depth of the magma chamber based on geochemistry, mineral chemistry, and Sr-Nd-Pb isotope chemistry. Lithos 388–389:106080

Li MM, Xu ZT, Ventura G, Pan XD, Han D, Gu GH, Yan DH, Pan B, Feng JQ (2021a) Geochronology and petrogenesis of early pleistocene dikes in the Changbai mountain volcanic field (NE China) based on geochemistry and Sr-Nd-Pb-Hf isotopic compositions. Front Earth Sci 9:729905

Li YB, Weng AH, Xu WL, Zou ZL, Tang Y, Zhou ZK, Li SW, Zhang YH, Ventura G (2021b) Translithospheric magma plumbing system of intraplate volcanoes as revealed by electrical resistivity imaging. Geology 49(11):1337–1342

Li ZS, Shan XL, Liu J, Zhang J, Liu ZH, Cheng CQ, Wang ZG, Zhao C, Yu HC (2023) Late Neoarchean TTG and monzogranite in the northeastern North China Craton: Implications for partial melting of a thickened lower crust. Gondwana Res 115:201–223

Liu JQ (1988) The Cenozoic volcanic episodes in northeast China. Acta Petrol Sin 4(1):1–10

Lloyd FE, Edgar AD, Ragnarsdottir KV (1996) LREE distribution in perovskite, apatite and titanite from South West Ugandan xenoliths and kamafugite lavas. Miner Petrol 57:205–228

Ludwig KR (2001) Squid (1.13b), A user's manual: Berkeley Geochronology Center Special Publication 2. -2003, ISOPLOT 3.0: A geochronological toolkit for Microsoft Excel 855

Lugmair GW, Marti K (1978) Lunar initial $^{143}Nd/^{144}Nd$: differential evolution of the lunar crust and mantle. Earth Planet Sci Lett 39(3):349–357

Ma JC, Tian Y, Zhao DP, Liu C, Liu TT (2019) Mantle dynamics of western pacific and East Asia: New insights from P wave anisotropic tomography. Geochem Geophys Geosyst 20(7):3628–3658

Mathieu L, Bouchard RA, Pearson V, Daigneault R, Barresi T (2016) The Coulon deposit: quantifying alteration in volcanogenic massive sulphide systems modified by amphibolite-facies metamorphism. Can J Earth Sci 53(12):1443–1457

McDonough WF, Sun SS (1995) The composition of the earth. Chem Geol 120:223–253

McDowell FW, McIntosh WC, Farley KA (2005) A precise $^{40}Ar–^{39}Ar$ reference age for the Durango apatite (U–Th)/He and fission-track dating standard. Chem Geol 214(3–4):249–263

Meffre S, Large RR, Scott R, Woodhead J, Chang ZS, Gilbert SE, Danyushevsky LV, Maslennikov V, Hergt JM (2008) Age and pyrite Pb-isotopic composition of the giant Sukhoi Log sediment-hosted gold deposit, Russia. Geochim Cosmochim Ac 72(9):2377–2391

Miles AJ, Graham CM, Hawkesworth CJ, Gillespie MR, Hinton RW, Facility EIM, (EIMF) (2013) Evidence for distinct stages of magma history recorded by the compositions of accessory apatite and zircon. Contrib Mineral Petr 166:1–19

Nardi LVS, Formoso MLL, Müller IF, Fontana E, Jarvis K, Lamarão C (2013) Zircon/rock partition coefficients of REEs, Y, Th, U, Nb, and Ta in granitic rocks: Uses for provenance and mineral exploration purposes. Chem Geol 335:1–7

Palma G, Barra F, Reich M, Valencia V, Simon AC, Vervoort J, Leisen M, Romero R (2019) Halogens, trace element concentrations, and Sr-Nd isotopes in apatite from iron oxide-apatite (IOA) deposits in the Chilean iron belt: Evidence for magmatic and hydrothermal stages of mineralization. Geochim Cosmochim Ac 246:515–540

Pan B, Silva S, Xu JD, Liu SJ, Xu D (2020) Late Pleistocene to present day eruptive history of the Changbaishan-Tianchi Volcano, China/DPRK: New field, geochronological and chemical constraints. J Volcanol Geotherm Res 399:106870

Pan LC, Hu RZ, Wang XS, Bi XW, Zhu JJ, Li C (2016) Apatite trace element and halogen compositions as petrogenetic-metallogenic indicators: Examples from four granite plutons in the Sanjiang region, SW China. Lithos 254–255:118–130

Paton C, Hellstrom J, Paul B, Woodhead J, Hergt J (2011) Iolite: Freeware for the visualisation and processing of mass spectrometric data. J Anal Atom Spectrom 26(12):2508–2518

Paton C, Hergt JM, Phillips D, Woodhead JD, Shee SR (2007) New insights into the genesis of Indian kimberlites from the Dharwar Craton via in situ Sr isotope analysis of groundmass perovskite. Geology 35(11):1011–1014

Paton C, Woodhead JD, Hellstrom JC, Hergt JM, Greig A, Maas R (2010) Improved laser ablation u-pb zircon geochronology through robust downhole fractionation correction. Geochem Geophys Geosys 11(3):1525–2027

Petcovic HL, Grunder AL (2003) Textural and thermal history of partial melting in tonalitic wallrock at the margin of a basalt dike, Wallowa Mountains, Oregon. J Petrol 44(12):2287–2312

Piccoli PM, Candela PA (2002) Apatite in igneous systems. Rev Mineral Geochem 48(1):255–292

Prowatke S, Klemme S (2006) Trace element partitioning between apatite and silicate melts. Geochim Cosmochim Acta 70(17):4513–4527

Ramos FC, Wolff JA, Tollstrup DL (2004) Measuring 87Sr/86Sr variations in minerals and groundmass from basalts using LA-MC-ICPMS. Chem Geol 211(1–2):135–158

Sakata S, Hirakawa S, Iwano H, Danhara T, Guillong M, Hirata T (2017) A new approach for constraining the magnitude of initial disequilibrium in quaternary zircons by coupled uranium and thorium decay series dating. Quat Geochronol 38:1–12

Schoene B, Bowring SA (2006) U-Pb systematics of the McClure Mountain syenite: thermochronological constraints on the age of the $^{40}Ar/^{39}Ar$ standard MMhb. Contrib Mineral Petr 151(5):615–630

Song XY, Lei JS (2023) Direct surface-wave tomography under Northeast China: New insights into 3-D crustal S-wave velocity structure and dynamics of intraplate volcanism. Phys Earth Planet Inter 334:106959

Sun CY, Cawood PA, Xu WL, Zhang XM, Tang J, Li Y, Sun ZX, Xu T (2022) In situ geochemical composition of apatite in granitoids from the eastern Central Asian Orogenic Belt: A window into petrogenesis. Geochim Cosmochim Ac 317:552–573

Sun JF, Yang JH, Zhang JH, Yang YH, Zhu YS (2021) Apatite geochemical and Srsingle bondNd isotopic insights into granitoid petrogenesis. Chem Geol 566:120104

Sun Y, Ying J, Zhou X, Shao JA, Chu Z, Su B (2014) Geochemistry of ultrapotassic volcanic rocks in Xiaogulihe NE China: Implications for the role of ancient subducted sediments. Lithos 208–209:53–66

Thompson JM, Meffre S, Danyushevsky L (2018) Impact of air, laser pulse width and fluence on U-Pb dating of zircons by LA-ICPMS. J Anal Atom Spectrom 33(2):221–230

Tian Y, Zhu H, Zhao D, Liu C, Feng X, Liu T, Ma JC (2016) Mantle transition zone structure beneath the Changbai Volcano: Insight into deep slab dehydration and hot upwelling near the 410 Km discontinuity. J Geophys Res Solid Earth 121:5794–5808

Tong XR, Liu YS, Hu ZC, Chen HH, Zhou L, Hu QH, Xu R, Deng LX, Chen CF, Yang L, Gao S (2016) Accurate determination of Sr isotopic compositions in clinopyroxene and silicate glasses by LA-MC-ICP-MS. Geostand Geoanal Res 40(1):85–99

Wang Y, Li CF, Wei HQ, Shan XJ (2003) Late Pliocene–recent tectonic setting for the Tianchi volcanic zone, Changbai Mountains, northeast China. J Asian Earth Sci 21(10):1159–1170

Warren I, Simmons SF, Mauk JL (2007) Whole-rock geochemical techniques for evaluating hydrothermal alteration, mass changes, and compositional gradients associated with epithermal Au-Ag mineralization. Econ Geol 102(5):923–948

Watson EB, Green TH (1981) Apatite/liquid partition coefficients for the rare earth elements and strontium. Earth Planet Sci Lett 56:405–421

Webster JD, Piccoli PM (2015) Magmatic apatite: A powerful, yet deceptive, mineral. Elements 11(3):177–182

Wei H (2014) Changbaishan Tianchi Volcano. Seismological Press, Beijing, pp 1–448. (in Chinese with English abstract)

Wei HQ, Zhao B, Chen ZQ, Yu HM (2021) Volcanic processes and magmatic evolution of Tianchi volcano, Changbaishan. Geol Soc Lond Spec Publ 510(1):15–26

White AJR, Chappell BW, Wyborn D (1999) Application of the restite model to the deddick granodiorite and its enclaves–a reinterpretation of the observations and data of Maas et al. (1997). J Petrol 40(3):413–421

Wolf MB, London D (1994) Apatite dissolution into peraluminous haplogranitic melts: An experimental study of solubilities and mechanisms. Geochim Cosmochim Ac 58(19):4127–4145

Xu S, Zheng G, Nakai SI, Wakita H, Wang X, Guo Z (2013) Hydrothermal He and CO2 at Wudalianchi Intra-plate Volcano, NE China. J Asian Earth Sci 62:526–530

Xu YG, Zhang HH, Qiu HN, Ge WC, Wu FY (2012) Oceanic crust components in continental basalts from Shuangliao, Northeast China: Derived from the mantle transition zone? Chem Geol 328:168–184

Xu ZT, Liu Y, Sun JG, Liang XL, Xu ZK (2020) Nature and ore formation of the Erdaohezi Pb-Zn deposit in the Great Xing'an Range. NE China Ore Geol Rev 119:103385

Yan DH, Li MM, Xu ZT, Sun LY, Ma F, Han D (2023) Genesis and Its Tectonic Significance of Heishigou Basaltic Lava Dyke in Tianchi Volcanic Area of Changbai Mountain. J Jilin Univ (Earth Sci Ed) 53(3):904–919

Yang B, Lin WL, Hu XY, Fang H, Qiu GG, Wang G (2021) The magma system beneath Changbaishan-Tianchi Volcano, China/North Korea: Constraints from three-dimensional magnetotelluric imaging. J Volcanol Geotherm Res 419:107385

Yang YH, Wu FY, Xie LW, Chu ZY, Yang JH (2014a) Re-evaluation of interferences of doubly charged ions of heavy rare earth elements on Sr isotopic analysis using multi-collector inductively coupled plasma mass spectrometry. Spectrochim Acta B 97:118–123

Yang YH, Wu FY, Yang JH, Chew DM, Xie LW, Chu ZY, Zhang YB, Huang C (2014b) Sr and Nd isotopic compositions of apatite reference materials used in U-Th–Pb geochronology. Chem Geol 385:35–55

Yatsuzuka S, Okuno M, Nakamura T, Kimura K, Setoma Y, Miyamoto T, Kim KH, Moriwaki H, Nagase T, Jin X, Jin BL, Takahashi T, Taniguchi H (2010) 14C wiggle-matching of the B-Tm Tephra, Baitoushan Volcano, China/North Korea. Radiocarbon 52(3):933–940

Ye XQ, Xu ZT, Sun LY, Li ZW, Li MM, Jia L (2022) The Genesis of Miocene tephrite in the Tiger Mountain volcanic area, Jilin Province, and tectonic implications. Earth Sci 49(4):1–14. (in Chinese with English Abstract)

Yuan F, Liu JJ, Carranza EJM, Zhang S, Zhai DG, Liu G, Wang GW, Zhang HY, Sha YZ, Yang SS (2018) Zircon trace element and isotopic (Sr, Nd, Hf, Pb) effects of assimilation-fractional crystallization of pegmatite magma: A case study of the Guangshigou biotite pegmatites from the North Qinling Orogen, central China. Lithos 302–303:20–36

Zhang B, Guo F, Zhang XB, Wu YM, Wang GQ, Zhao L (2019) Early Cretaceous subduction of Paleo-Pacific Ocean in the coastal region of SE China: Petrological and geochemical constraints from the mafic intrusions. Lithos 334–335:8–24

Zhang JJ, Zheng YF, Zhao ZF (2009) Geochemical evidence for interaction between oceanic crust and lithospheric mantle in the origin of cenozoic continental basalts in east-central China. Lithos 110:305–326

Zhang ML, Guo ZF, Liu JQ, Liu GM, Zhang LH, Lei M, Zhao WB, Ma L, Sepe V, Ventura G (2018) The intraplate Changbaishan volcanic field (China/North Korea): A review on eruptive history, magma genesis, geodynamic significance, recent dynamics and potential hazards. Earth-Sci Rev 187:19–52

Zhang XB, Guo F, Zhang B, Zhao L, Wu YM, Wang GQ, Alemayehu M (2020) Magmatic evolution and post-crystallization hydrothermal activity in the early Cretaceous Pingtan intrusive complex, SE China: records from apatite geochemistry. Contrib Mineral Petr 175(4):1–18

Zheng Y, Xu Z, Zhao Z, Dai L (2018) Mesozoic mafic magmatism in North China: Implications for thinning and destruction of Cratonic lithosphere. Sci China Earth Sci 61:353–385. (in Chinese)

Zhou JB, Wilde SA, Zhao GC, Han J (2018) Nature and assembly of microcontinental blocks within the Paleo-Asian Ocean. Earth-Sci Rev 186:76–93

Zhu H, Tian Y, Zhao D, Li H, Liu C (2019) Seismic structure of the Changbai intraplate volcano in NE China from joint inversion of ambient noise and receiver functions. J Geophys Res Solid Earth 124:4984–5002

Zou HB, Fan QC, Yao YP (2008) U-Th systematics of dispersed young volcanoes in NE China: Asthenosphere upwelling caused by piling up and upward thickening of stagnant Pacific slab. Chem Geol 255(1–2):134–142

Zou HB, Fan QC, Zhang HF, Schmitt AK (2014) U-series zircon age constraints on the plumbing system and magma residence times of the Changbai volcano, China/North Korea border. Lithos 200–201:169–180